2023

# Characterizing Air Plasma Sprayed Aluminum Oxide Coatings for the Protection of Structures in Lunar Environments

Perla Latorre Suarez
*University of Central Florida*

## STARS Citation

Latorre Suarez, Perla, "Characterizing Air Plasma Sprayed Aluminum Oxide Coatings for the Protection of Structures in Lunar Environments" (2023). *Electronic Theses and Dissertations, 2020-*. 1600.
https://stars.library.ucf.edu/etd2020/1600

# CHARACTERIZING AIR PLASMA SPRAYED ALUMINUM OXIDE COATINGS FOR THE PROTECTION OF STRUCTURES IN LUNAR ENVIRONMENTS

by

PERLA CRISTAL LATORRE-SUAREZ
B.S. University of Central Florida, Orlando FL, 2021

A thesis submitted in partial fulfillment of the requirements
for the degree of Master of Science
in the Department of Mechanical and Aerospace Engineering
in the College of Engineering and Computer Science
at the University of Central Florida
Orlando, Florida

Spring Term
2023

Major Professor: Seetha Raghavan

# ABSTRACT

Wear-resistant ceramic and ceramic composite coatings are significant to provide durability and support long-duration missions to the moon's surface for rovers, landers, robotic systems, habitats, and many other components. On the Lunar surface, structural components are continuously exposed to lunar dust projectiles that can cause protective coating delamination around the affected area, of protective coatings and this may not be physically visible. Ceramic coatings, composed of alumina, present excellent resistance to different types of wear due to their high strength and hardness as well as the ability to protect structural components from regolith impacts, wear, and abrasive damage. Air Plasma Spray (APS) already plays a vital role in the aerospace industry by protecting engine structures against wear, friction, corrosion, high temperatures, and harsh environments. In this study, an Inconel 738 substrate was grit blasted, following a 100- $\mu$m layer bond coat, and a 200-$\mu$m layer of alumina was deposited using APS. Prior to performing destructive experiments, the microstructure and characteristics of the APS alumina coating were studied and analyzed. Scanning electron images were collected to observe the anisotropic properties of the APS alumina coating. The X-Ray diffraction measurements demonstrated that $\alpha$-phase and $\gamma$-phase are the dominant phases present in the APS alumina coating. The roughness of the APS alumina coating was measured with a profilometer, resulting in an average of 4.063 $\mu$m. The surface energy plays a role in enhancing the adhesion of the regolith particles to the surface of the components and systems used for lunar exploration. In this study, the surface energy had an average advancing contact angle of 61.13°, relating to low surface energy. Artificial damage was introduced by indenting the coating using Rockwell and Vickers indenters. The hardness of the APS alumina coating was measured around the different indentation locations. The measured Vickers hardness values at 1000 gf and 2000 gf were found to be 0.2913 GPa and 0.5677 GPa, respectively. An initial Rockwell hardness value of 38.9 was found and was reduced to 22.5 after two surrounding indentations were applied to the coating. Results showed that the Rockwell hardness value decreases as the number of indentations around the initial indent increases. The fracture toughness of the APS alumina coating was calculated using the cracks formed during the last two Rockwell indentations and was found to be 2.48 and 2.95 MPa$\sqrt{m}$. Considering the optical properties of the alumina, piezospectroscopic (PS) measurements were taken to detect the underlying coating delamination and determine the mechanical properties of the APS alumina coating. The peak shifts from the characteristic alumina peaks revealed the underlying damage, quantifying the effect of projectiles on the overall coating integrity. The multifunctional properties of alumina, utilized in the studies performed here, have offered a unique means for understanding the durability of a material with high spatial and stress resolution.

*I dedicate this work to my parents, my brother, and Shakia for always supporting me, inspiring me, and never leaving me alone with this journey. I would also like to dedicate this effort to my advisor, Dr. Raghavan, for believing in me and supporting my ideas when they seemed impossible.*

# ACKNOWLEDGMENTS

This material is based upon work supported by the National Aeronautics and Space Administration under Grant No. 80NSSC21M0309 issued through the NASA Office of STEM Engagement. The author Latorre-Suarez would like to acknowledge the Florida Space Grant Consortium (FSGC) for Masters Fellowship support. Mr. Frank Accornero and Dr. Mary McCay (Applied Research Laboratory, Florida Institute of Technology) are acknowledged for their support with the air plasma spray coating deposition. The authors also thank Dr. Ranajay Ghosh from University of Central Florida for use of instrumentation for microscopy studies.

# TABLE OF CONTENTS

# LIST OF FIGURES

# LIST OF TABLES

# CHAPTER 1
# INTRODUCTION

The detrimental effect of lunar dust on structural components is a current limiting factor to return to the lunar surface. The term “lunar regolith” describes the layer of particles on the Moon’s surface generated by meteoritic impacts and is comparable to terrestrial volcanic ash [1, 2]. Lunar dust contains multiple minerals, particle sizes, and shapes varying across the location on the Moon. The Moon’s geography is divided into the Highland and the Mare regions. The Highland region is the elevated area at the lunar surface, the lighter areas visible to the naked eye, whereas the Mare region is the dark area visible to the naked eye [3]. The particle size distribution and mineralogical composition of the lunar soil vary at the different locations on the lunar surface [3, 4]. Grain shapes are highly variable and range from spherical to extremely angular geometries, as illustrated in Figure 1.1. It has been reported that more than a quarter of lunar soil is made of agglutinates or fused soil, as well as a small fraction of impact-generated glasses and breccias. In order to determine the relative amount by volume of the lunar regolith, a process called modal analysis has been used by researchers to expand the estimation of the chemical composition of the soil as well as the chemical data for the individual mineral [1]. The basaltic-rich mare, also known as the Maria region, contains dark basalts. The Highlands are rich in Anorthosite, whereas the regolith is deeper in the older highlands and has lighter-colored feldspar-rich rocks. The location across the lunar surface is considered through the experimental process of this work, accounting for the different particle sizes, shapes, and mineralogical compositions. The regolith mechanical properties can cause a wide variety of damage to the structure of the components and systems used for lunar exploration. From the Apollo missions, the maximum and minimum temperatures monitored were 390 K to 104 K, and it was determined that structures should be well insulated [3]. Other factors, such as gravity, the lack of atmosphere, and the absence of a magnetic field in the lunar environment, have been demonstrated to influence the behavior of the lunar regolith particles.

The low electrical conductivity of the lunar regolith allows individual dust grains to retain an electrostatic charge. During the day, conductivity can increase with surface temperature, infrared and ultra-violet radiation [5]. The dust is electrically charged, enhancing its adhesive properties and promoting wear and abrasive degradation on the vehicles and components brought on-site [2]. During the day, the lunar regolith is positively charged since the conductivity can increase with surface temperature and infrared and ultraviolet radiation. During the night, the particles are negatively charged due to the interaction with solar wind electrons [6]. The adhered particles can affect the integrity of the components and systems used for lunar exploration. For instance, the rovers are rolling, and part of its structure is constantly exposed to bombardments of small regolith particulates. Mechanical adhesion was due to the barbed shapes of the dust grains. Studies about the effects of the lunar regolith within the components and systems used for lunar exploration have been conducted since the Apollo missions. Observations from the Apollo mission stated that the lunar regolith affected the lunar module, clogged mechanisms, interfered with instruments, caused radiators to overheat, and tore up spacesuits [5].

Understanding the lunar regolith dynamic behavior and composition is essential to be able to characterize the forces and variables that can affect and damage the components used for lunar exploration. Furthermore, it is also critical to understand the lunar transport and material abrasion behavior. The lunar surface is commonly exposed to ballistic ejection from impact craters and along with gravitational creep and this tends to replace newer soils on top of older soils. Further studies on the lunar regolith showed that lunar regolith can be shock-lifted at low pressures, reflecting that the lunar regolith is porous and the pores collapse rapidly during the passage of the compressive phase of the shock wave. From the six Apollo missions that landed on the lunar surface, the effects of the lunar dust in Extra-Vehicular Activity has been studied demonstrating that the effects can be sorted into nine categories: vision obscuring, false instrument readings, dust coating and contamination, loss of traction, clogging of mechanisms, abrasion, thermal control problems, seal failures, and inhalation and irritation [7]. Results from Apollo 11 and Apollo 12 distinguished four groups based on texture, porous and unshocked, shock-compressed but still porous, glass-welded, and thermally metamorphosed [1].

The lunar soil, is a mixture of different types of particles. These particles can be broadly classified into five categories: mineral fragments, pristine crystalline rock fragments, breccia fragments, glasses of various kinds, and agglutinates. Each of these types of particles has unique characteristics that contribute to the overall composition of the lunar soil. The most common minerals found in the lunar regolith are plagioclase feldspar, clinopyroxene, orthopyroxene, and olivine [8].

These minerals have been identified through various methods, including spectroscopic analysis and sample returns from the Apollo missions. While the different mineralogic compositions of the lunar regolith are not explicitly considered in the study, the hardness of each mineral and chemical compound present in the soil is considered. However, the hardness of each mineral and chemical compound is considered since it is an important parameter that can damage the surface of the structures used for lunar exploitation. The hardness and mechanical properties of the lunar regolith particles allows us to ensure that the ceramic coating will adhere properly and provide adequate protection against the harsh lunar environment.

## 1.1 Needs for Lunar Dust Mitigation

Previous lunar missions, such as the Apollo mission, demonstrated damages caused by the lunar regolith particulates. Researchers have investigated the lunar dust deposition after lunar landing, accounting for external factors such as ambient temperature and solar angle incident. The results demonstrated that the dust deposition was mainly induced by the landing process and factors such as rover movement though the analysis and rover movement route [9]. Lunar structural components are constantly exposed to high-velocity lunar dust projectiles causing delamination around the affected area. Micrometeoroid size range from 10 nm to 150 $\mu$m in radius with masses of $10^{-18}$ to $10^{-8}$ kg impact the Moon at an airspeed range of 10 to 72 km/s, delivering their kinetic energy to a point below the lunar surface at a depth comparable to the size of the impactor [10, 11]. Low-velocity impacts of the lunar regolith particles have a range velocity of around 1 - 230 cm/s [11].

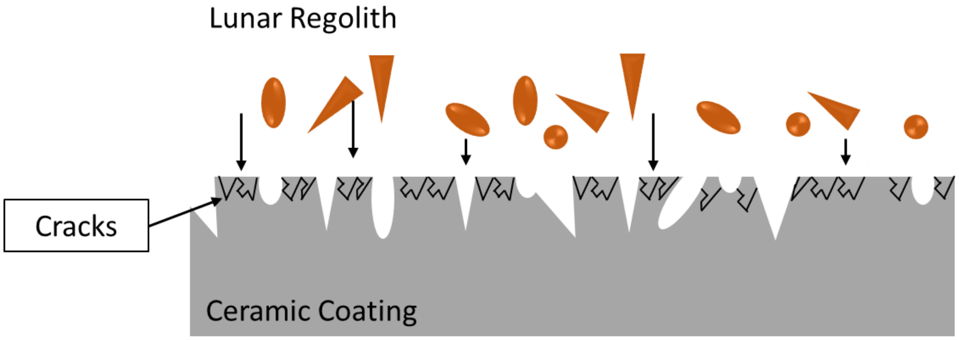

Figure 1.1: Different particle size and shapes affect the integrity of the lunar vehicles at different velocities. When the lunar regolith bombard the lunar vehicles, internal and plastic deformation are developed.

The impact response of laminated composites have been previously studied with a low velocity of 1.2 - 2.8 m/s and compared with static indentations tests with velocities of $0.2*10^{-4}$ m/s [11]. The results from the study demonstrated a correlation between low velocity impact and quasi-static responses.

The wear damage is categorized in different types, erosive, abrasive, and sliding and rolling wear. The erosive wear is due to stream of particles or liquid droplets when they hit a surface. When the particles hit a brittle surface, a brittle fracture takes place, for ductile materials, fatigue and shear failure occurs. However, the abrasive wear is caused by hard or sharp particles. During the abrasive wear, the loss material is dominated by brittle fracture or fatigue [12]. The sliding and rolling wear is a dominant mechanism that causes a loss of material as well as shear and fatigue fracture. In the absence of an atmosphere or any form of erosion or fluid motion, the particles are not sorted by size, and they maintain their abrasive properties [11]. Abrasion is critical since it affects any material that moves or has a sealing surface. Abrasion is one of the four basic types of wear or physical mechanism for material removal or displacement. Previous studies have customized tips fabricated from terrestrial counterparts of lunar minerals for scratching tests [13]. The results helped to apply standards when selecting materials for developing dust mitigation strategies for lunar components and systems [13].

Different mitigation methods available and studied during previous studies are essential to determine the right approach to develop a material to protect the lunar components and systems from the harsh behavior of the lunar regolith particles. Different strategies such as dust generation avoidance, passive mitigation, active mitigation, and dust tolerant design have been studied and developed. The dust generation limits the generation of dust during system operations. The passive mitigation involves coatings and finishing under a surface treatment or performed to a material to prevent dust adhesion [14]. Considering the electrostatic adhesion of the lunar regolith, multiple investigations have studied super-hydrophobic materials such as the lotus leaf [15]. Reducing the material's surface energy for particle adhesion mitigation is a strategy used in nature with the lotus plant [16]. Researchers have applied the "Lotus Effect" to evaluate the efficacy for lunar dust mitigation [16]. The lotus leaf coating has been developed and successfully applied into a variety of materials. The coating has demonstrated itself to be high durable and thermally stable in vacuum over a wide temperature range [14]. However, its durability under the lunar extreme environment is still under review. Other passive mitigation approaches include laser texturing, electrostatic discharge coatings, and peel away coating. Active dust mitigation technologies aim

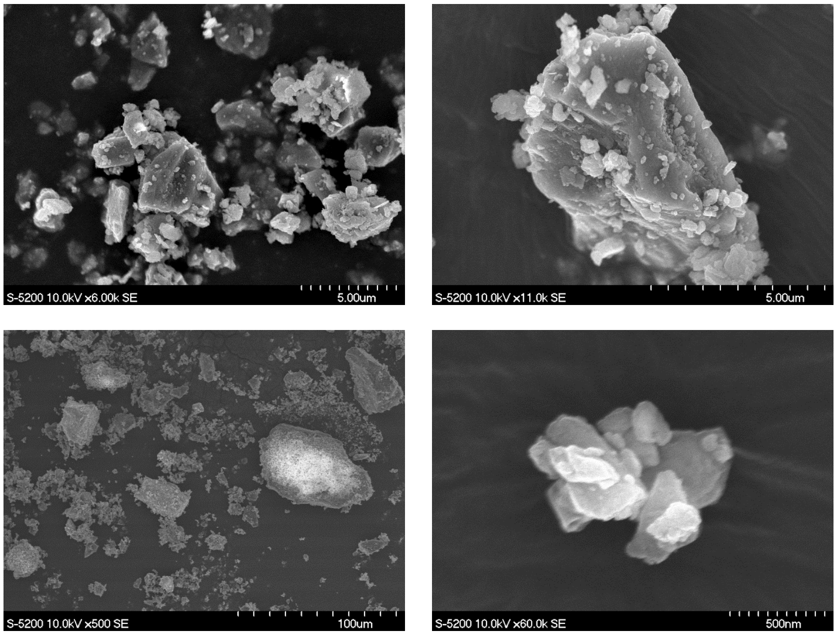

Figure 1.2: SEM images show the surface physical properties, particle size, and shapes of the lunar simulants from the Mare region.

to remove the dust that has already adhered to the surface. The active dust mitigation include electrodynamics dust shield, nylon/fiberglass brush, pressurized gas, vibration, electron gun, and magnetic roller [14]. Other proposed solutions for lunar dust active mitigation include, electrostatic curtains to repel charged dust, magnets to attract dust containing iron, use of rechargeable sticky surfaces, surface treatment to reduce dust adhesion, development of dust-resistant material and seals. Studies have demonstrated that laser ablation of polyimide substrates can reduce the surface adhesion [17].

## 1.2 Ceramic Coatings to Protect Components from Lunar Regolith

In space exploration, durability and longevity are critical factors to consider when designing components for long-duration missions. Wear-resistant ceramic coatings and ceramic composites play an essential role in providing the required durability to critical components, such as rovers, landers, robotic systems, habitats, and other spacecraft hardware. As previously discussed in this chapter, the lunar environment poses significant challenges for spacecraft hardware due to the presence of dust, regolith, and sharp rocks, which can cause abrasive wear, erosion, and impact damage. Ceramic coatings and composite materials offer excellent wear resistance, which can protect hardware from abrasive and impact wear, extending their useful life in the harsh lunar environment. For instance, ceramic coatings can be applied to critical components such as wheels, joints, and bearings to protect against wear and reduce friction, increasing the life of these components. Ceramic composite materials can also be used to manufacture structural components such as frames and supports, which require high strength, stiffness, and wear resistance. The Artemis mission to the Moon's surface is a prime example of a long-duration mission that will require highly durable components. The mission will require robust hardware that can withstand the harsh lunar environment for extended periods. The use of wear-resistant ceramic coatings and composite materials can significantly contribute to achieving this objective, increasing the mission's chances of success and reducing the risk of mission failure due to component wear and damage.

Ceramic materials, such as alumina, have several desirable mechanical properties, including high strength and excellent retention of strength at both low and high temperatures [18]. These properties make them suitable for use in the lunar environment, where temperature fluctuations can be extreme. However, wear and abrasive resistance are also important properties to consider, and factors such as particle size, shape, surface treatment, and dispersion can affect these properties [18]. Previous studies have studied the addition of titania with alumina and have demonstrated that it increases the porosity and decreases the microhardness of the material [19]. To improve the mechanical properties of alumina, researchers have added cubic boron carbide, which has been shown to increase the material's hardness and toughness [20]. Studies have also explored the effects of particle size and weight percentages on composite materials, with nanoscale particles demonstrating significant improvements in mechanical properties [21]. In addition to these material modifications, researchers have also explored different deposition methods, such as spark plasma sintering, to create high-performance ceramic materials with strong mechanical properties. These efforts will continue to improve our understanding of how to engineer ceramic materials for use in demanding environments such as space [22].

### 1.2.1 Thermal Spray of alumina as Protective Coating

Due to their high strength and hardness, alumina ceramics are demonstrated to have an excellent resistant to different types of wear. Alumina coatings are also demonstrated to provide the substrate corrosion protection and thermal protection. Previous studies have demonstrated that $Al_2O_3$-Zr$O_2$ exhibits better wear resistance than pure alumina [23]. Different alumina coating manufacturing methods have been analyzed during previous studies, including High-Velocity Oxygen Fuel [24],

Table 1.1: List of researched ceramics with the mechanical properties to protect structures at the lunar surface.

| **Parameters** | Zirconia | Alumina | Zirconia toughened alumina | Boron nitride | Silicon nitride | Boron carbide | Silicon carbide |
|---|---|---|---|---|---|---|---|
| **Young's modulus (Gpa)** | 200 | 375 | 358 | 46.9 | 140-310 | 450 – 470 | 410 |
| **Fracture Toughness (MPA*m^1/2)** | 7 ∼8 | 4 | 5 | - | 3.1 – 6.2 | 2.9 – 3.7 | 4.6 |
| **Poisson's ratio** | 0.31 | 0.22 | 0.23 | - | 0.24 – 0.27 | - | 0.14 |
| **Density (g/cm^3)** | 5.6 | 3.89 | 3.96 | 2.3 | 2.2 – 3.4 | 2.52 | 3.1 |

Physical Vapor Deposition [25], Chemical Vapor Deposition [26], and Air Plasma Spray (APS) [18]. Early studies conducted at our research laboratory tested the behavior of alumina particles applied onto substrates with different thicknesses through APS [18]. The cold spray process of alumina has demonstrated a significant impact on corrosion resistance [27], wear resistance [28], and well-bonded substrate interface [29]. APS alumina has demonstrated the potential to protect the surface to which they are applied. Besides their principal role of providing protection against abrasion and wear caused by lunar dust, materials such as alumina, with high mechanical strength, both compressive and flexural, and high hardness, can help to improve the durability of the structures during lunar missions by providing electrical, chemical and thermal protection.

Thermally sprayed ceramic materials, for instance, are commonly used to protect metallic surfaces from corrosion, wear, and high temperatures. The mechanical properties of these materials are critical to ensure durability in harsh environments. Further, alumina is frequently used for thermally sprayed applications due to its high strength and wear resistance. These coatings have inconsistent thin lamellae, or "splats," which form during rapid solidification of the impacted molted droplets. As a result, thermally sprayed coatings have imperfect bonds at the interface of the splats and the substrate [30]. Moreover, APS coating's micro-structural composition provides a variety of stress concentrations in the form of horizontal and vertical micro-cracks [18]. The APS alumina coatings are mainly composed of $\alpha$- and $\gamma$-phase alumina due to the high temperatures and cooling process experienced during the deposition process [31]. The $\alpha$-phase alumina contains chromium ion impurities that make the particles a photo-luminescent and stress-sensitive material.

## 1.3 Overview of the Research

**There is a need for wear-resistant ceramic coatings that can significantly contribute to protecting structures from damage caused by the lunar regolith.** In order to address the complications described above for lunar exploration, this work focuses on designing a ceramic coating with the ability to protect the mechanical components. Thermally sprayed alumina is analyzed and investigated in this study. The limited access to materials and equipment during lunar exploration is also considered in this study. Alumina possesses multifunctional properties with the ability to monitor the structural integrity of the components through photo-luminescence. Here, we integrate the multifunctional properties of the alumina coating as a secondary focus. A series of experiments have been performed to study and characterize the manufactured alumina coatings. Lunar dust is one of the challenges affecting the vehicles by exposing them to lunar regolith projectiles damaging the surface of the spacecraft.

Chapter 2 discusses the theories of the techniques and instruments used to determine the mechanical properties of the alumina coating. Considering the wear and abrasive damage caused by the lunar regolith and lunar dust electrostatically adhered particles, Quasi-static Vickers and Rockwell hardness experiments were conducted to simulate low-impact velocity impact of regolith particles in this work. The indentation rate for both experiments was correlated with the relationship between quasi-static indentation rate and low-velocity impacts. X-ray diffraction (XRD) and piezospectroscopy (PS) were the optical techniques used to non-destructively evaluate the ceramic coatings. In this work, XRD was performed to determine the phase composition of the thermally sprayed alumina coating. Due to the phase change composition that the alumina particles undergo through the thermally spraying process, the phase composition needs to be analyzed. Multiple studies have shown that the main alumina phases present in the thermally sprayed alumina coating are $\alpha$- and $\gamma$-phase. However, studies have debated that $\alpha$-phase alumina is the most desirable phase present in thermally sprayed coatings due to their stability and hardness. The PS technique was employed to monitor the integrity of the coating utilizing the optical properties present in $\alpha$-phase alumina. PS has been used to detect underlying damages through measurements of residual stresses. Pairing the indentation experiments and the optical properties of the coating, will allow us to determine the mechanical properties of the thermally sprayed alumina coating after the indentations are performed.

Chapter 3 presents the description of the experimental methods and manufacturing process used to investigate the properties of the thermally sprayed alumina coatings. The alumina particles were deposited using APS due to their versatility in being implemented onto complex and larger scale structures. The deposition parameters were investigated and analyzed from previous investigations. The spraying parameters may affect the microstructural composition and integrity of the coating. The topography and surface energy of the coating has been investigated using a profilometer and a contact angle goniometer. The profilometer was used to measure the roughness distribution across the surface of the APS alumina coating. The contact angle goniometer was used to study the surface energy of the coating and determine whether the regolith particles will have strong adhesion forces at the surface of the APS coating. These two studies are major since the adhered particles may cause wear and abrasive damage on the coating while the system is performing its tasks at the lunar surface. A scanning electron microscope (SEM) was used to observe the microstructural characteristics of the APS alumina coating. The indentation experiments simulated low-impact micro- and macro-meteoroid of regolith particles at the surface of the APS alumina coating. Due to the thermal and residual stresses provoked during the thermal spraying process, the stress values were observed as the surface was indented. The low-velocity impacts, hardness, and other mechanical properties of the APS alumina coating were determined utilizing Vickers and Rockwell hardness experiments. The Rockwell hardness experiment was performed on the A scale. The Vickers hardness experiment was performed at two loads to determine any effects of low-velocity impact micro-meteoroids at the surface of the APS coating. For the Rockwell hardness experiment, three indentations were performed at different locations in the samples to determine the hardness average value and study the effect of multiple low-velocity impacts at the surface of the APS alumina coating. The hardness was calculated by measuring the indented diameter and determining the indented depth. Furthermore, PS was used to demonstrate the APS alumina coating's multifunctionality in determining stress change and other mechanical properties as the surface of the coating is damaged.

Chapter 4 discusses the results obtained for each study conducted to characterize the APS alumina coating for protection of the lunar exploration systems and components. The roughness and surface energy of the APS alumina coating was measured prior to the indentations being performed. Studies have demonstrated that the roughness of the coating may affect the hardness measurements of the tested material. High surface energy and roughness of the coating may increase the adhesion and affect the integrity of the APS coating. This information also contributed to the results collected during the indentation experiments. In this study, the roughness of the coating did affect the hardness from the Vickers measured. The SEM images demonstrated micro-cracks developed during the APS process, as well as splats and unmelted particles, affecting the phase composition of the APS alumina coating. The Rockwell indentation experiment was studied and analyzed paired with the PS technique to determine underlying damages developed during the indentation process and the effects of the indentations. The results demonstrated in this work are correlated with the low-velocity impacts of the lunar regolith, as well as the wear and abrasive damage developed during lunar exploration. The hardness values are measured and compared with each other. The hardness and mechanical properties of the APS were affected by each indentation. Considering the distance of the indentation, they were also demonstrated to affect each other. This work supports the investigation and design of materials for lunar and other planetary exploration.

# CHAPTER 2

# THEORY OF TECHNIQUES TO DETERMINE THE MECHANICAL PROPERTIES OF CERAMIC MATERIALS

Considering the extreme environment at the lunar surface, materials resistant to wear and abrasive damage need to be considered. In order to determine the mechanical properties of the material, multiple experiments, such as indentation and other characterization techniques were considered. Indentation techniques are utilized to characterize the properties of a material. For ceramic coatings micro- and nano-indentations are commonly used to determine the hardness and modulus of elasticity of the coating. Chapter 2 discusses the theory and the techniques used to characterize and test the APS alumina coating for lunar exploration.

## 2.1 Mechanical Testing Methods to Characterize Ceramic Materials

Hardness measurements are often used to characterize the mechanical properties of APS alumina coatings. There are several methods used to measure the hardness of coatings, including the Vickers hardness test, the Rockwell hardness test, and the Knoop hardness test. The hardness values of ceramic coatings have been demonstrated to have a great effect on the wear of the materials considering the plastic deformation while fracture of toughness is a dominant factor in wear involving brittle fracture [32]. The Knoop hardness test is a microhardness test that is often used for measuring the hardness of thin coatings such as APS alumina coatings. This test involves applying a pyramidal diamond indenter with a very small load onto the surface of the coating and measuring the length of the resulting impression. The hardness value is calculated based on the load and the length of the impression. Considering that the knoop hardness is more sensitive to the near-surface properties due to the shape of the indenter, previous studies have correlated the damage caused by the wear with the measured Knoop hardness values [33].

The hardness measurements are performed to determine the material's deformation and durability. Indentation methods, such as Rockwell, Vickers, and Knoop, are frequently used to measure the mechanical properties of ceramic coatings [34]. In this experiment, the Rockwell hardness test was performed as the samples were manufactured using a metallic substrate underneath the thin APS coating. The Rockwell test determines the hardness by measuring the depth of penetration of an indenter under a large load. Previous studies performed impact indentation experiments to simulate wear and fatigue on the coating and observed that the wear at the macrocracks increases with the number of impacts before coating delamination starts [35, 36, 37]. Early studies have demonstrated that only a few strong ceramics can withstand the Rockwell A-scale hardness test. The Rockwell superficial hardness test with a total load of 15 kg, 30 kg, and 45 kg have been performed on ceramics to study their macro-hardness [38].

Previous studies used Vickers instrumentation to analyze the ceramic's reduced Young's Modulus as a function of the diamond indenter's Young's Modulus and Poisson's ratio [39, 40]. Other methods use relationships of applied force, depth sensing, or stiffness for determining mechanical properties [39, 40, 41, 42]. However, the applicability of such methods for acquiring these characteristics is limited to nano-indentation techniques due to the cracking and brittleness of ceramic materials. For macro-indentation techniques, previous studies used Rockwell indentation to determine the interfacial toughness of ceramics' thermal barrier coatings through direct calculations [43]. Nonetheless, these traditional methods for determining mechanical properties have negative consequences that could affect measurement acquisition. One illustration is sink-in and pile-up effects induced during experimentation. Sink-in is when the area directly surrounding the indent is lower than the rest of its surroundings, while pile-up is the opposite. Pile-up has been shown to cause over-estimations of both Young's Modulus and hardness due to the approximated contact area being drastically smaller than the actual value [44].

Indentation methods are commonly been used to measure the adhesion properties of the coating. Most tests aim to introduce a stable interfacial crack to make it propagate under controlled conditions and model this process to determine adhesion. Adhesion failure is often considered as a cracking event in which can be described by an interfacial toughness parameter, which along with the mechanical properties of the coating and substrate, can be used to predict onset and rate of propagation of failure. For thin films, nanoindentation is used to measure the mechanical properties of a coating (e.g. young's modulus, hardness and fracture of toughness and interfacial toughness). For brittle materials, the buckling interfacial failure is more likely than the shear-induced delamination when the coating is relatively tough compared with the interface [45]. Previous studies have also used finite element analysis to study the crack formation of ceramic materials. It was demonstrated that cracks form during indentation hardness tests of ceramic materials. The study demonstrated that the "pop-in phenomenon" on indentation hardness test results for ceramic materials cannot be ignored. The indentation experiments can also be used to determine the elastic-plastic properties and fracture toughness of ceramic materials [46].

### 2.1.1 Vickers Hardness Test

The Vickers hardness test is commonly used for measuring the hardness of APS alumina coatings. This test involves applying a pyramidal diamond indenter with a specified load onto the surface of the coating and measuring the diagonal lengths of the resulting impression. The hardness value is calculated based on the load and the area of the impression, as shown in Figure 2.1. Studies have demonstrated that the Vickers hardness was influenced by the spray parameters such as spray distance, amperage, and transverse rate [47]. Previous studies demonstrated that the Vickers hardness increases with decreasing applied indenter load, explained in terms of Kick's law as well as relating it to the microstructural characteristics of APS alumina coatings and the elastic recovery during the indentation. The study also demonstrated that the measured Vickers hardness values are related to the special microstructure and high anisotropic behavior of the APS coating [48]. It has been shown that the Vickers hardness value for the $\alpha$-alumina range from 1800 to 2300 [49]. However, as-sprayed coatings, typically only $\gamma$-alumina is present, but no data on the hardness of highly dense sintered samples are available as the material would transform into $\alpha$-alumina. The values of dense, thermally sprayed coatings can be as high as 1500 [49]. Vickers hardness have also been

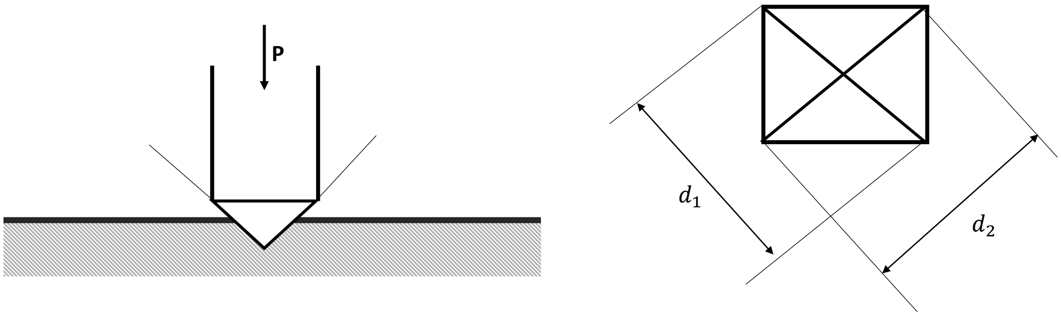

Figure 2.1: Vickers hardness and geometry of the square pyramid indenter.

performed in APS composite coatings with different heat treatments, the results demonstrated that the microstructure changes were reflected in the average Vickers hardness of the coatings [50].

### 2.1.2 Rockwell Hardness Test

The Rockwell hardness test is another commonly used method, which involves applying a specified load onto the surface of the coating using a conical or spherical indenter and measuring the depth of the resulting impression. The hardness value is calculated based on the load and the depth of the impression. Previous studies have used Rockwell scale A to perform scratch tests by sliding the indented over the sample and progressively increasing the load once the indenter was over the sample surface. The multipass test allowed to verify for damage accumulation effects [51]. APS alumina-titania coatings were tested under superficial Rockwell hardness with a load of 15N where

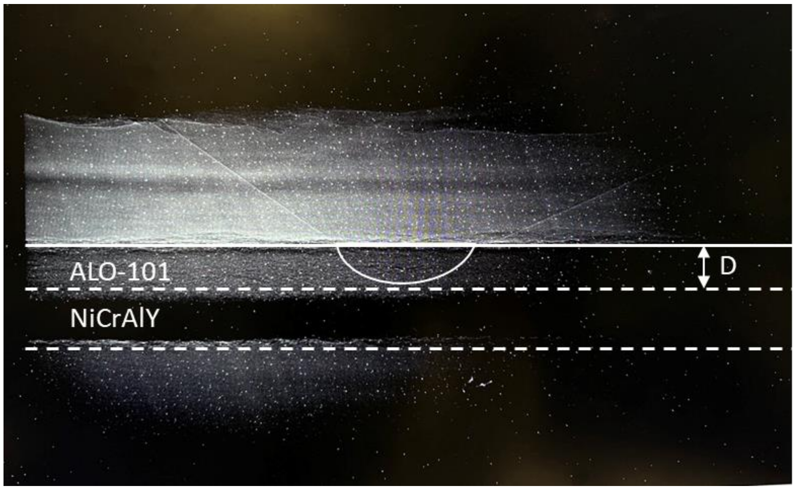

Figure 2.2: Rockwell hardness is determined by the displacement of the indenter within the coating/material.

the hardness values ranged from 47 to 62.8 [47]. The Rockwell hardness of carbon steel coated with APS alumina has been tested under the Rockwell hardness A (HRA) scale, the hardness value found to be 92.6 [52]. However, the exact hardness value can vary depending on factors such as the thickness of the coating, the substrate material, and the testing conditions.

## 2.2 Optical Techniques to Non Destructively Evaluate the Ceramic Materials

Optical techniques have been explored to non destructively determine the integrity of the APS alumina coating. X-Ray Diffraction (XRD) has been considered to determine the composition of the thermally sprayed coatings. Moreover, spectral peak variation can be tailored to determine mechanical properties and quantify residual stresses. Piezospectroscopy (PS), for instance, is an optical technique that has demonstrated the ability to collect high spatial resolution measurements of underlying damage [53]. Moreover, Raman spectroscopy has been used to determine stress distributions among the microstructure of ceramic composites [54]. Spectroscopic methods such as Raman has been used to evaluate the residual strain after ballistic performance of composite materials [55]. However, optical laser-based techniques have not been established for measuring mechanical properties beyond stress characteristics of ceramic materials. In this study, we aim to investigate pairing indentation methods with optical techniques for acquiring mechanical properties to study low-velocity impact on coatings.

### 2.2.1 X-Ray Diffraction

XRD analysis is a nondestructive technique that provides detailed information about the crystallographic structure, chemical composition, and physical properties of a material. X-rays are shorter wavelength electromagnetic radiation that are generated when electrically charged particles with sufficient energy are decelerated. Each phase of the material produces a unique diffraction pattern due to the material's specific chemistry and atomic arrangement. XRD has been considered to determine the residual stresses of thermally sprayed coatings. However, in the lower energy reflective mode the XRD analysis can be limited to the surface layer, and depth profiling is a challenge [56]. Changes in peak position indicate the expanding crystal lattice that gives the thermal expansion properties. High temperature XRD can unveil reaction kinetics, intermediate phases in a reaction, or high-temperature phases that decomposes at lower temperatures [57]. The temperature increment leads to enhancement in intensity of XRD peaks due to the growth of alpha-phase. Multiple researchers have demonstrated that the main phases present in the phase composition of APS alumina coatings are $\alpha$ and $\gamma$-alumina [57, 58].

### 2.2.2 Photoluminescent Piezospectroscopy

The piezospectroscopic (PS) effect is based on the fact that when a crystalline material experiences an applied stress, strain in the lattice affects the transition energy between electronics or vibrational bands [59]. This method has been developed as a portable system in our lab that allows for in-situ and non-contact stress detection to effectively diagnose the stress state of a surface [60]. The main phases present in APS aluminum oxide are $\alpha$ and $\gamma$-phases. Due to the chromium ion impurities present in $\alpha$-alumina, coating stress can be investigated with photoluminescent piezospectroscopy (PLPS). When $\alpha$-alumina is excited with a light source, it emits photons from two distinct energy levels resulting in doublet peaks known as R-lines. When a force is applied on the coating, or in the case of stress relaxation, the changes in the crystal lattice induce an emission wavelength shift. The PLPS technique is used here to provide high spatial resolution measurements of the underlying stress and damage from indentations. Spectral peak variation can be tailored to determine mechanical properties and quantify residual stresses. Researchers [53, 35] utilized piezospectroscopy (PS) to measure underlying damage of ceramic coatings. Studies have used PLPS to study the residual stresses of thermally sprayed coatings, demonstrating that the macro-stress caused by the thermal mismatch between the substrate and the coating decreases from the interface to the top surface

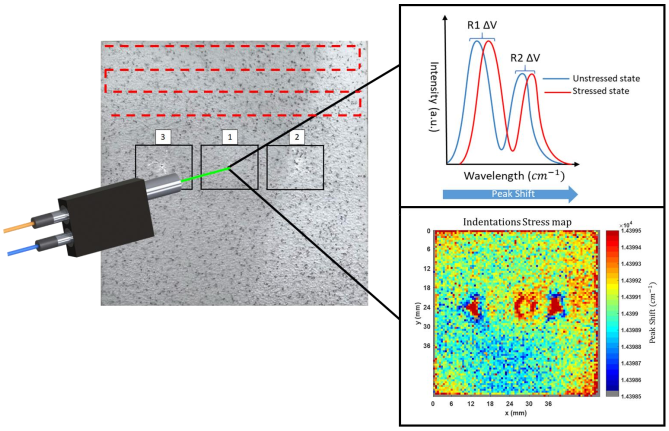

Figure 2.3: Piezospectroscopic technique.

[61]. Nano-indentation was performed in this experiment [61] to determine the mechanical properties of the coating. However, they did not correlate the PLPS measurements with the mechanical properties of the coating using indentation techniques. To circumnavigate such complications, in this work, indentation methods have been paired with optical techniques for acquiring mechanical properties. This is a unique method that have been explored in this study, and will be discussed in Chapter 4.

# CHAPTER 3

# DESCRIPTION OF EXPERIMENTAL METHODS TO INVESTIGATE PROPERTIES OF AIR PLASMA SPRAY ALUMINUM OXIDE

Various experimental methods to investigate ceramic coatings can be limited and complex due to their brittle behavior. Understanding the ceramics will enable us to understand wear, abrasive, impact damage, and the mechanical properties of the ceramic coating. In this study, APS alumina coatings have been selected for the protection of structures against the effects of regolith wear and impact damage. As discussed in Chapter 1, alumina has excellent resistance to different types of wear. In order to investigate the performance of the APS alumina coatings, test specimens were developed through the APS of alumina onto a metallic substrate. Section 3.1 discusses the manufacturing process of the APS alumina coating. Thermally sprayed ceramic coatings have been widely used to protect structures from different damage factors, such as wear and abrasivion. APS coatings are considered for this study due to its background in protecting structures and its application in the aerospace industry. Section 3.2 discusses the equipment and experiments performed to study the microstructural composition and topography of the APS alumina coating. A profilometer and contact angle goniometer were used to determine the roughness of the surface and surface energy of the APS alumina coating. The roughness and surface energy of the surface of the coating influence the adhesion force of the lunar regolith on the coating. A scanning electron microscope

(SEM) was used to collect high-resolution images of the coating and study the micro-cracks formed during the APS deposition process. Section 3.3 discusses the relationship between the quasi-static indentation experiments and the low-velocity impacts from the lunar regolith. Studies have demonstrated the relationship between quasi-static indentation and low-velocity impact experiments. The following section 3.4 discusses the Vickers and Rockwell indentation experiments performed to simulate the low-impact velocities of the lunar regolith. Vickers hardness experiments were performed to simulate the micro-impacts and determine the micro-hardness value of the APS alumina coating. The Rockwell hardness experiments were performed to simulate the macro-impacts of the lunar regolith particles and determine the macro-hardness of the coating. The hardness, fracture toughness, brittleness, and other mechanical properties will be determined through the Vickers and Rockwell hardness experiments. Section 3.5 discusses the parameters and properties of the optical techniques used to evaluate the phase composition and monitor the integrity of the coating. X-ray diffraction (XRD) was used to determine the phase composition of the APS alumina coating. Most of the APS alumina particles change their phase composition during the APS process, affected by the spraying parameters. Piezospectroscopy (PS) was used to monitor the integrity of the coating after each indentation was performed to determine the residual stresses across the APS alumina coating.

## 3.1 Sample Manufacturing and Particle Deposition Method

Thermally sprayed alumina coatings have been widely used in industrial components. The thermally sprayed coatings are considered wear, corrosion, and abrasive resistant, as well as thermally or electrically insulative coatings to improve the surface characteristics of the components. The air plasma spray (APS) deposition method is a versatile method that can be implemented in space components. The APS method is cost-effective and can be applied to complex structures and aerospace applications. APS is commonly used for the protection of high-temperature gas turbine components. In this study, the alumina coating was deposited using the APS method. The technique uses the energy contained in a thermally ionized gas to melt fine powder particulates on a surface such that they adhere and agglomerate to produce a coating [62, 63]. Ceramic materials are mostly considered for APS deposition due to their higher hardness value due to their smaller grain size, resistance to wear, and low incidence of defects [63]. Previous studies have demonstrated that the roughness of the substrate needs to be around 4-5 $\mu$m to ensure mechanical interlocking between the sprayed coating and the substrate [62]. However, over-blasting the surface can reduce the mechanical interlocking by rounding off the sharp peaks and affect the adhesion between the coating and the substrate [62].

Factors such as the spraying parameters, bond coat, and substrate compatibility are considered to ensure the quality of the thermally sprayed coating. The spraying parameters of the thermally sprayed coating play a critical role in the integrity of the sprayed material. Previous studies have demonstrated that hydrogen flow affects the porosity of the sprayed coating. Moreover, the Argon

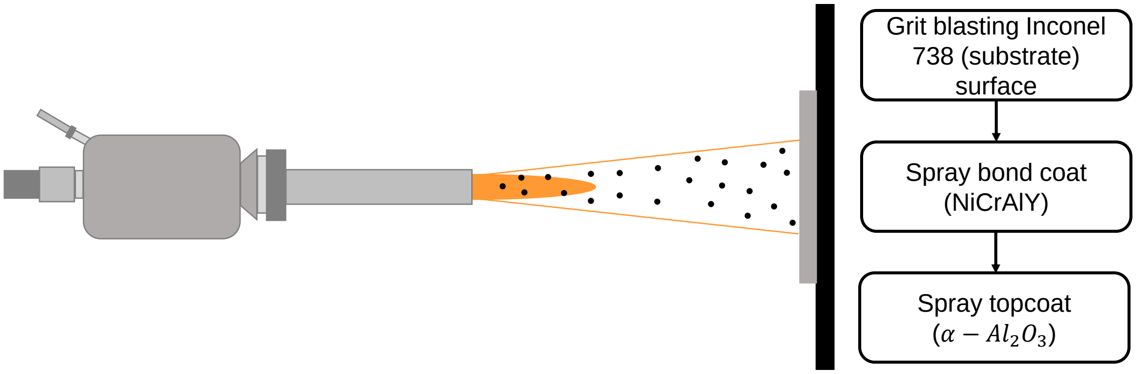

Figure 3.1: Schematic of coating deposition using air plasma spray.

gas flow is responsible for accelerating the powder particles. Studies demonstrate that with faster particle velocity, the melting behavior of the powder will be affected by the dwell time of the particles and this provides lower coating thicknesses [64]. The plasma current parameter affects the particle velocity. When the pumping rate is higher, the particles' velocity, as well as the particle surface temperature is higher. The power rate can also affect the particles' behavior. Decreasing the plasma power decreases the deposition efficiency and increases the porosity. The injection angle is another parameter that could affect the porosity of the coating by lowering the droplet temperature and minimizing the number of droplets [64]. Other research further investigated the effect of the coating porosity by measuring it with digital image analysis method [65]. They demonstrated that porosity is critical to ensuring quality characteristics to understand the microstructure and properties of thermally sprayed materials. During the plasma spray process, the pores and micro-cracks can generate from different sources, such as entrapped gases, incomplete filling from the rapidly solidified splats, and the shrinking of the splats during rapid solidification [65]. In our study, the parameters of input power, stand-off distance, and powder feed rate were considered and analyzed from previous literature.

For this experiment, an Inconel 718 substrate with a thickness of 635 $\mu$m was machined into 50.8 by 50.8 mm (2 x 2 inch) coupons. These tiles were grit blasted with silica to increase surface roughness, providing a physical interlocking mechanism for the plasma sprayed particles to adhere. The bond coat with a layer thickness of 100 $\mu$m (Praxair, NI-164) and a topcoat layer of 200 $\mu$m aluminum oxide (Praxair, ALO-101, medium particle size of 45 $\mu$m) was air plasma sprayed onto the substrate. The bond coat has been demonstrated to promote adhesion and oxidation resistance within the ceramic coating and the substrate [66] and improves the durability of the deposited ceramic topcoat by stimulating attachment between the first layer of the plates and the surface of the bond coat [66]. The spray gun was positioned 76.2 mm (3 inches) away from the sample's surface and sprayed at a horizontal speed of 300 mm/s with a vertical offset of 3 mm. The particles were ejected using a 900 A current and a voltage of 43.9 V. The primary spraying gas used was Argon (54 SLM), while the secondary gas was helium (44 SLM).

## 3.2 Topography of Air Plasma Spray Aluminum Oxide

### 3.2.1 Profilometry

The spraying parameters play a critical role on the integrity of the coating and may affect characteristics such as the roughness of the APS alumina coating. Previous studies have demonstrated

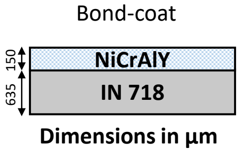

| Properties | Value |
|---|---|
| Chemical composition | 22% Cr<br>10% AL<br>1% Y |
| Particle Size | -106 µm / +45 µm |

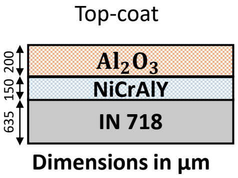

| Properties | Value |
|---|---|
| Chemical composition | 99% $Al_2O_3$ |
| Particle Size | -45 µm +5 µm |
| Density | 1.1 g/cc |

Figure 3.2: Schematic with information on the particles used to deposit the topcoat (ALO-101) and bond coat (NiCrAlY) on the surface of the sample.

that surface roughness is affected by the spraying parameters (e.g. stand-off distance and plasma power) [67]. The particle melting increase with power, more melting particles will lower the surface roughness of the coating [68]. Furthermore, the roughness of the coating may also increase the adhesion forces of the regolith particles entrapped at the surface of the APS alumina coating. To measure the surface roughness of the APS coating, profilometry (FRT CWL) measurements were collected to determine the roughness of the APS alumina ceramic coating. Roughness measurements were taken on three samples with coating thicknesses of 122, 128, and 150 $\mu$m. A scanning area of 5 x 5 mm, 250 lines, and 1000 points per line with a resolution of 20.08 $\mu$m per line, and 5.005 $\mu$m for points per line were taken for each sample.

### 3.2.2 Contact Angle Goniometry

Contact angle goniometry is used to determine the surface energy and surface tension of the coating. Previous studies analyzed the effect of surface energy and demonstrated that low surface energy is desired for the surface of the lunar components since it will decrease the adhesion forces between the lunar regolith and the component [69]. Other researchers performed experiments on hydrophobic and hydrophilic materials to study the adhesion forces of stimulants of lunar regolith onto the surface of the materials [70]. The results demonstrated that fewer particles adhered to the hydrophobic materials, compared to the hydrophilic material. Contact angle goniometry measurements were taken on samples with APS alumina coating thicknesses of 122, 128, and 150 $\mu$m. For this experiment, the material to wet the surface of the coating used to measure the surface tension was water, with a controlled volume of around 7.89 $\mu$L. The maximum angle that the samples were tested was 60°at a rate of 2°per second. During this experiment, the samples were placed under a needle to drop the material onto the surface of the APS alumina coating. The volume of the material was measured and controlled. The system was calibrated with and without a sample to ensure data accuracy.

### 3.2.3 Scanning Electron Microscope

Scanning electron microscope (SEM) allow to collect high resolution images of the specimen. SEM images of the APS alumina samples were collected to observe the microstructural characteristics of the coating prior inducing indentation damage. For the SEM images, a small piece of coating was added to a sample holder and coated with conducting material (Au-Pd) to allow the microscope beam to collect images and decrease the signal to noise ratio. The voltage and current used for this experiment was 10 kV and 20 $\mu$A. The images were observed using different magnifications considering the surface area and anisotropic composition of the coating.

### 3.3 Justification of Quasi-Static Indentation Simulating the Low-Velocity Regolith Impact

Low-velocity impacts of regolith particles are part of human and robotic exploration activities. Considering the low ambient pressure and the low gravity environment, the regolith particles may have an impact speed of around 4 - 230 cm/s [71]. Researchers have studied the outcome of low velocity collision into simulated regolith with a range of 1 - 100 cm/s. The impact response of laminated composites have been previously studied with low velocity of 1.2 - 2.8 m/s and compared with static indentation tests with velocities of 0.2x$10^{-4}$m/s [72]. The study demonstrated a correlation between low velocity impact and quasi-static responses. Further studies were performed and demonstrated that there is no distinct difference between static indentation and low velocity impact test, indicating that static indentation can be used to represent low velocity experiments[73]. In this study, Vickers hardness experiments were performed with a an indentation speed of 70 $\mu$m/s [74], and the Rockwell hardness experiments were performed with an indentation speed of 0.2 mm/s [75].

## 3.4 Indentation Experimental Studies

In order to understand how the micron-projectiles can affect the ceramic protective coating, an initial study using static experiments was performed. The Rockwell indentation method allows us to determine the hardness of the materials by measuring the depth of penetration of the indenter under a defined mechanical load. Previous studies performed impact indentation experiments to simulate wear and fatigue on the coating and observed that the wear at the macrocracks increases with the number of impacts before coating delamination starts [36]. Researchers have studied the outcome of very low velocity, 1-100 cm/sec, collisions into simulated regolith [76]. Their results demonstrated that the impact study resulted in small dust ejecta produced by the impacts. In this study, Vickers hardness experiments were performed with a dwell time of 10 seconds [74], and the Rockwell hardness experiments were performed with an indentation speed of 0.2 mm/s [75].

### 3.4.1 Vickers Hardness Test

As discussed in Chapter 2, Vickers hardness is commonly used to study multiple properties of thermally sprayed coatings. In order to study the micro hardness and fracture of toughness of the APS alumina coating, Vickers hardness tests were performed. Using the micro hardness values, it will allow to characterize the resistance of the ceramic to deformation, densification, displacement, and fractures. Vickers hardness experiments were performed onto an APS alumina coating with a layer thickness of around 311.8 $\mu$m. Following the ASTM-E384 [74], the indentations were performed diagonally from each other. Two indentation load of of 1000 gf and 2000 gf were performed at the surface of the APS alumina coating. Considering the low impact velocity of the lunar regolith, the displacement rate was 60 $\mu$m/s.

### 3.4.2 Rockwell Hardness Test

Rockwell hardness (HR) test was performed in this experiment considering the metallic substrate's material. For this experiment, a spheroconical indenter with a tip made of diamond with an angle of 120 °was utilized to perform the indentations at the APS ceramic coating. The preliminary force applied was 98 N, with a dwell time of 1 second and a contact velocity of 0.2 mm/s. The total load applied for each indentation was 588.4 N, as indicated in the ASTM E-18 for HR scale A (HRA). The ASTM E-18 states a minimum distance of three times the diameter of the indented region between indentations. In this experiment, the indentations were performed at 12.7 mm to ensure no effects from the indentations around each other. The first indentation was performed in the middle of the sample, and the other two indentations were performed at the right and left sides of the first indentation.

## 3.5 Optical Techniques used to Evaluate Mechanically Tested Air Plasma Sprayed Aluminum Oxide

APS aluminum oxide is mainly composed of $\gamma$- and $\alpha$ -phase particles developed during the particle deposition process. In order to confirm the phase composition of the coating, XRD measurements were taken on APS alumina coatings with an inclination range of 10°- 100 °, and inclination rate of 0.01 degree/seconds with a speed duration of 5 seconds, a voltage of 40 kV and a current of 44 mA. Furthermore, the alpha-phase of aluminum oxide have demonstrated photoluminescent properties with the ability of sensing stress. Sprectral acquisition data was performed using photoluminescent piezospectroscopy (PLPS) to provide high spatial resolution measurements of the underlying stress and damage from the indentations [77]. Previous studies have demonstrated that the this method has the ability of determining underlying damage around indented regions [78, 37] as well a providing the mechanical properties of the material [79]. The piezospectroscopic (PS) measurements were collected using an 532 nm Nd:YAG laser. The data was collected with a laser power of 10 mW and 10 ms exposure time. Each map was collected after each indentation with a resolution of 600 $\mu$m and a map size of 50 x 50 mm. Spectral acquisition data was performed using a portable Piezospectroscopic (PPS) instrument that uses a fiber collection spectrometer (Pixis 100, Princeton Instruments) [77, 60]. The specimens were tested with a laser power of 10 mW. Exposure time for spectrum acquisition was 10 ms to avoid saturation of the charged couple device. A resolution of 200 $\mu$m and 50 spectral positions were collected per indentation. The data was deconvoluted and fitted using pseudo-Voigt functions and a linear base removal [80].

# CHAPTER 4
# OPTICAL MEASUREMENTS CHARACTERIZING THE MECHANICAL RESPONSE OF AIR PLASMA SPRAY ALUMINUM OXIDE FROM LOW VELOCITY IMPACT OF REGOLITH PARTICLES

Considering the extreme environments, low ambient pressure, and the low gravity environment on the lunar surface, it is important to conduct experiments to characterize materials for structural protection and determine whether their mechanical properties are able to sustain the lunar surface environment. Regolith particles may have an impact speed of around 4 - 230 cm/s [71, 76]. In this study, indentation experiments were performed to represent the low velocity impacts of the lunar regolith particles onto the APS alumina coating with the parameters described in Chapter 3. Exploration activities at the lunar surface will include components and systems causing motion that involves the interaction with the regolith particulates. This will result in wear and abrasive damage to the vehicle structures and mechanical systems. Section 4.2 of Chapter 4 discusses the results obtained from the topographical and micro-structural compositions of the APS alumina coating. Instruments such as scanning electron microscopic images, profilometry, goniometry, and X-ray diffraction, were used to determine the microstructural composition of the APS alumina coating described in Chapter 3. The porosity, roughness, surface energy, surface tension, and phase composition are analyzed for coatings of various thicknesses. As discussed in previous chapters, these characteristics affect the integrity of the coating and may increase the damage and adhesion properties of the lunar regolith particles and the protective coating.

Utilizing the indentation tests, the section 4.2 discusses the hardness and fracture toughness of the coating. In addition, this section highlights the interaction among indentations representing multiple impacts and how this relates to the damage progression on the APS alumina coating. The Vickers and Rockwell hardness experiments are discussed and analyzed to determine their mechanical properties using the $\alpha$-phase multifunctional photoluminescent properties. Piezospectroscopy was employed to monitor the structural integrity of the coating after the hardness measurements to determine internal crack propagation and delamination across the APS alumina coating. Vickers hardness indentation was performed simulating micro-impacts while the Rockwell hardness test was performed to simulate the macro-impacts of the lunar regolith onto the coating. Section 4.3 discusses the residual stress of the indented APS coating utilizing the optical properties of the coating. In this section, the optical properties of the coating allow for monitoring and quantifying its integrity after multiple indentations. As a secondary emphasis, the indentation experiment coupled with the measurement of optical response allows for multiple coating properties such as the residual stresses, fracture toughness, brittleness, modulus of elasticity, and other mechanical properties to be established. This demonstrates a pathway for efficient mechanical property determination from a single test.

## 4.1 Microstructural Characterization of the Air Plasma Sprayed Alumina Coating Before Indentation

As discussed in Chapter 3, the roughness and surface tension of the APS coating plays a vital role in determining the microstructural characteristics of the thermally sprayed coating and its protective behavior. Therefore, the selection of material and processing parameters of the APS alumina coating studied here was based on the intended use and the desired surface characteristics. The roughness of a ceramic coating also affects its performance properties, such as its wear resistance and durability. Moreover, previous studies have also demonstrated that larger roughness values have greater stress concentrations [81]. Studies have also demonstrated that roughness affects the hardness measurement process. Therefore, considering thin, rough coatings that require smaller depth indentation, and increasing the number of data collection can contribute to the hardness measurement [81]. The roughness of the APS alumina coating can also contribute to the amount of regolith particles that are entrapped at the surface of the APS coating. This is because the roughness and surface tension values at the surface of the APS coating can affect and contribute to the adhesion forces between the ceramic coating and the lunar regolith. The surface energy of lunar regolith and materials used for lunar surface exploration systems and vehicles play a role in protecting their integrity. The lower surface energy of materials is preferred to decrease the adhesion strength between the regolith particles and the material's surface and decrease the amount of regolith particles attached to the coating surface [16, 14].

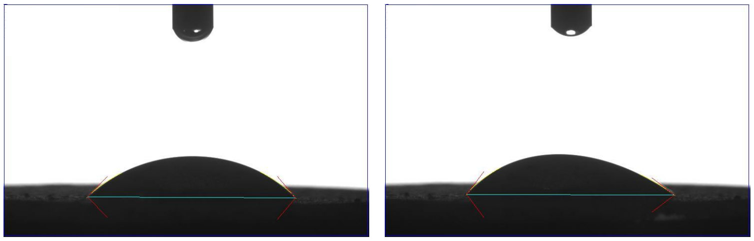

Layer thickness 128 µm at 0°

Layer thickness 128 µm at 52.6°

| Layer Thickness (µm) | Surface Roughness (µm) | Advancing Contact Angle |
|---|---|---|
| 122 | 4.171 | 71.36 |
| 128 | 3.714 | 52.6 |
| 150 | 4.304 | 59.44 |

Figure 4.1: Goniometry for 128 $\mu$m coating, and the surface roughness and advancing contact angle for three APS alumina coatings.

### 4.1.1 Relationship Between APS Alumina Layer-Thickness and Roughness

The APS alumina coating with thicknesses of 122, 128, and 150 $\mu$m have roughness values of 4.171, 3.714, and 4.304 $\mu$m, respectively, as listed in Figure 4.1. The roughness of the coating did not show a distinct trend or correlation with the coating thickness. However, the roughness of thermally sprayed coatings is affected by other spraying parameters. In this case, the number of passes, and other factors, such as the cooling rate or room temperature, might have affected the deposition process for the coatings. Due to the variation in roughness of the alumina coating, the measured hardness at different locations may also vary. The study demonstrated that the layer-thickness of the coating does not have a direct relationship with the roughness of the coating. Further studies need to be performed to determine the parameters that will contribute to improve the roughness of the coating for better adhesion between he regolith and the coating.

### 4.1.2 Relationship Between APS Alumina Layer-Thickness and Advancing Contact Angle

The surface tension of APS alumina coatings is challenging to measure directly, as it is influenced by several factors, such as the coating microstructure, porosity, and surface roughness. The high surface tension of alumina can result in a reduced ability of the molten particles to wet the substrate surface during the spray process, leading to the formation of elongated or splat-shaped rather than spherical microstructures. On the other hand, the surface energy can be measured using techniques such as contact angle measurements or surface energy analysis. The measured surface energy of the APS alumina was calculated to be around 32.6 mN/m. The surface energy of APS alumina coatings can be affected by the surface roughness, porosity, and chemical composition of the APS alumina coating. In general, a higher surface energy can result in better wettability and adhesion of the coating to other materials, while a lower surface energy can result in reduced wettability and adhesion. Therefore, the surface energy of an APS alumina coating is a property to be assessed for specific applications where adhesion or wetting behavior is critical. Overall, while surface tension is not a relevant property for APS alumina coatings, surface energy is a factor in determining the performance and behavior of the APS alumina coating.

The advancing contact angles of the APS alumina coating with thicknesses of 122, 128, and 150 $\mu$m, were measured with the goniometer. The advancing contact angle results of 71.36, 52.60, and 59.44, respectively, as displayed in 4.1. The measured advancing contact angles for the APS alumina coating were smaller than 90 degrees. Therefore the APS alumina coatings is a hydrophilic material. Although the samples with a coating thickness of 122 $\mu$m had a measured advancing contact angle of 71.36 degrees, compared with the samples with coating thicknesses of 128 and 150 $\mu$m, no discernible correlation was observed. However, more studies with more layer-thicknesses need to be performed to determine whether any effects of coating thickness, since the results did not have a correlation between the layer thickness values and the advancing contact angle. The surface energy is correlated with the adhesion force between the lunar regolith and the surface of the coating. In this study, the results demonstrated that the APS alumina coatings have high surface energy due to the small advancing contact angle. Therefore, the surface energy of the APS alumina coating needs to be reduced in order to decrease the adhesion force between the surface of the coating and the regolith particles.

### 4.1.3 Microstructural and Phase Composition of the APS Alumina Using SEM and XRD

The plasma spraying process and parameters are known to influence the mechanical properties of alumina ceramic coating. In order to observe the surface, topographical features, and microstructure of the APS alumina coating, SEM images provided a higher magnification and resolution. Figure 4.2 displays the morphology of the APS coating, showing an uneven and porous surface. The SEM images in Figure 4.2 exhibited unmolten or semi-unmolten particles due to the rapid solidification process during the APS deposition. However, previous studies have demonstrated that increasing the spraying plasma power can cause the melting of the particles and become better flattened on the substrate in the form of splats [82]. The images in Figure 4.2 also exhibited crack strips at the interface caused by the low bonding strength due to the poor melting. The quenching

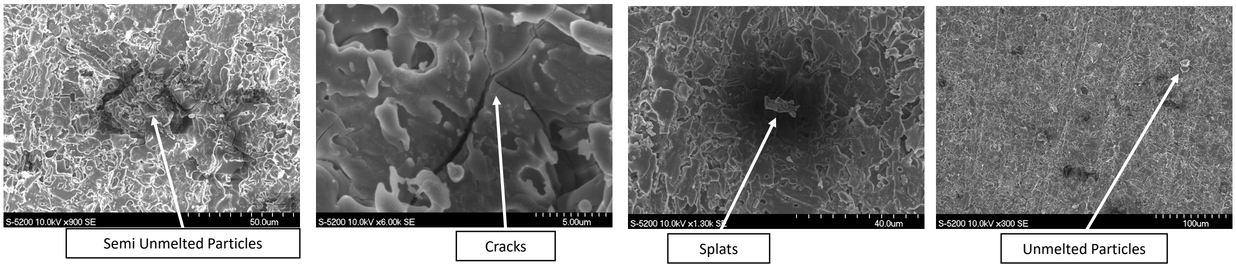

Figure 4.2: The SEM images show the physical and anisotropic properties of the APS alumina.

stress and interlaminar stress generated during the spraying process can also cause defects [82]. Previous studies have demonstrated that the pores size range is from 1 - 50 $\mu$m [83]. The pores are formed as a result of multiple factors such as the overlapping of sprayed particles, volume shrinkage of molten particles, and deposition of gas in the molten particles.

XRD measurements were collected to confirm the presence of $\alpha$-phase alumina. Figure 4.3 displays the phase composition of the APS alumina coating. As expected from previous studies [31, 67, 82], the main phases present in the APS alumina coating were $\alpha$- and $\gamma$-phase. The presence of the $\alpha$- and $\gamma$-phase is due to multiple factors, including the post-deposition cooling rate. The presence of the $\gamma$-phase is due to the quick solidification of molten alumina. The APS coating is determined to be composed of both stable $\alpha$-phase and cubic metastable $\gamma$-phase. However, with increased plasma power input, the amount of the metastable phase increases [67]. The sharp peaks corresponding to the $\gamma$-alumina in the diffraction pattern indicate a good degree of melting of the particle. However, partial oxidation occurs during the APS deposition process of the particles.

Aluminum oxide can provide high corrosion resistance and could prevent corrosion of the metal substrate [58]. Researchers have studied the effects of the spray parameters and particle properties with respect to the phase formation during the spray process [84]. The study demonstrated that the larger particle sizes in diameter and the presence of unmelted core in particles may have a greater fraction of $\alpha$-phase present in the microstructural composition of the coating [84]. However, other studies have demonstrated that $\alpha$-phase alumina is often the most desirable phase due to its high corrosion resistance and hardness [85], as well as its improvement in the mechanical properties of the APS alumina coating [86]. Both studies [85, 86] implemented chromium particles to help stabilizing the desirable $\alpha$-phase particles. Although, in this study the volume fraction of the $\gamma$-phase alumina is greater than $\alpha$-phase, further experiments will be performed to increase the presence of the $\alpha$-phase alumina particles. The hardness of the particles are vital to ensure that the APS alumina coating sustain the impact of the regolith particles. The $\alpha$-phase has exhibited to have multifunctional properties, such as, the $\alpha$-phase alumina contains chromium ion impurities that make the particles photoluminescent. The $\alpha$-phase coating can be implemented to monitor the integrity of the components and systems used for lunar exploration.

## 4.2 Hardness and Fracture Toughness Results

The indentation parameters simulating low-velocity impacts of regolith particles were described in Chapter 3. In this study, Vickers hardness experiments were performed with displacement rate of 60 $\mu$m/s and a dwell time of 10 seconds [74], and the Rockwell hardness experiments were

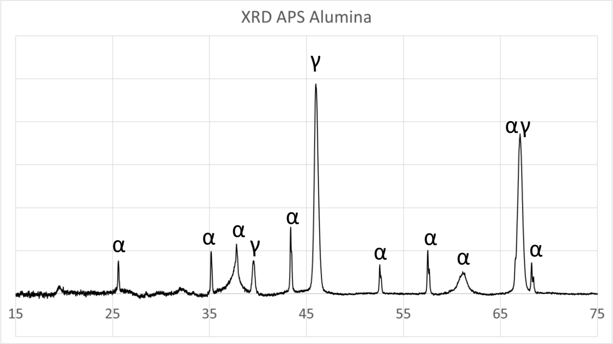

Figure 4.3: X-Ray Diffraction patters of the APS alumina coating.

performed with an indentation speed of 0.2 mm/s [75]. The tested loads for the Vickers test are classified as micro-impacts and the Rockwell test as macro-impacts. Vickers hardness was performed on the plasma sprayed alumina coating to determine the effects of the low-velocity impact and the APS alumina coating microhardness, as well as other properties such as fracture toughness. Vickers hardness was performed on an APS alumina-coated sample with a layer thickness of around 312 $\mu$m and no bond coat. Due to the thickness of the coating, it had a roughness of about 4.91 $\mu$m. A load of 1000 gf, considered micro-hardness, was applied into the coating with a displacement rate around 60 $\mu$m/s and a dwell time of 10 seconds [74], as shown in Figure 4.4. However, due to the high roughness of the coating, the indentation was not found under Vicker's microscope. A second indentation with a load of 2000 gf, considered macro-hardness, was performed diagonally from the first indentation. Due to the high roughness of the surface of the coating, the indentation was not found under a microscope. The samples were observed under a high-resolution optical microscope. In order to confirm the indented areas, the samples were

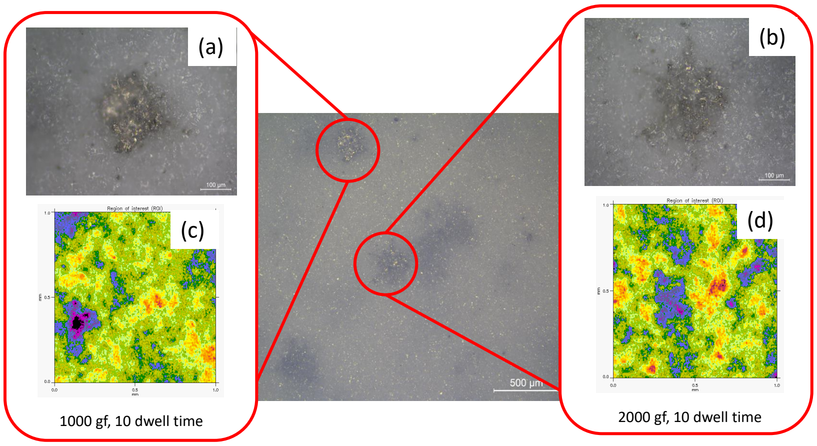

Figure 4.4: Vickers hardness results (a) 1000 gf with a dwell time of 10 seconds (b) 2000 gf with a displacement of 60 $\mu$m.

placed under a profilometer (FRT Mark 3) using high resolution. ImageJ was used to measure the indentation area and calculate the Vickers hardness using equation 4.1, following the ASTM E384. The Vickers hardness value for 1000 gf (9.8 N) was 0.2913 GPa, and for 2000 gf (19.6 N) was 0.5677 GPa. Previous studies determined the Vickers hardness of APS alumina coatings and demonstrated to be around 2.04 GPa [39]. Researchers have demonstrated that the hardness of thermally sprayed coatings depend on the spraying conditions and morphology of the powder feed-stock, which can affect the mechanical properties of the coating [87]. Potential factors to affect the Vickers hardness of the APS alumina coating analyzed in this investigation involves the high roughness value of the coating.

Indentation experiments are categorized in nano-, micro-, and macro-indentations. The macro-indentations are those performed at loads greater than 1000 gf. Accounting for the macro-impact particles in the coating, the Rockwell experiment was performed. Compared with the Vickers hard-

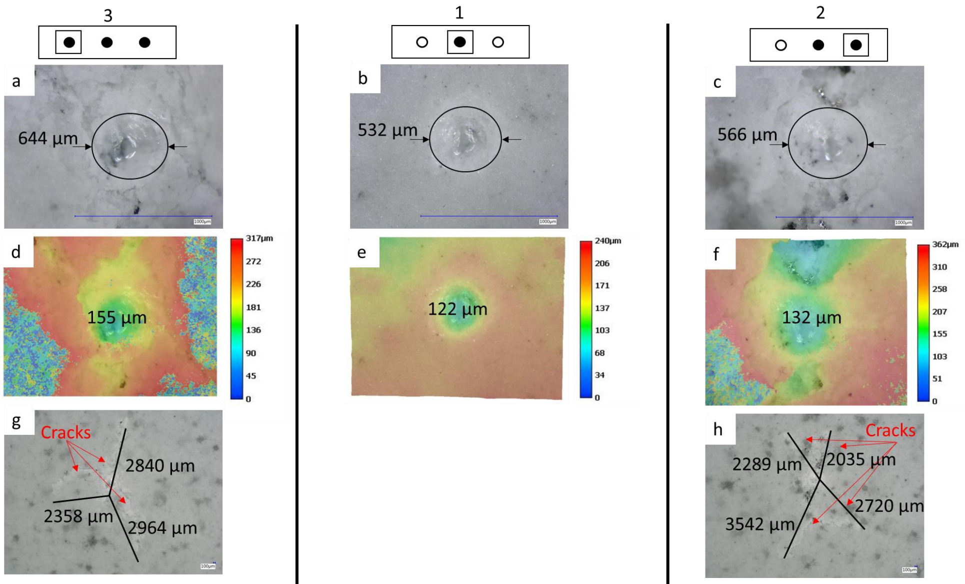

| | | | |
|---|---|---|---|
| **Calculated hardness (HRC)** | 22.5 | 38.95 | 33.75 |
| **Calculated toughness (MPa$\sqrt{m}$)** | 2.92 | N/A | 2.48 |
| **Calculated plastic radius (µm)** | 4.83 | N/A | 5.23 |

Figure 4.5: (a-c) Microscopic images of all indentations with their respective diameters, (d-f) Maps of all indentations showing their respective depths, and (g-h) Microscopic images showing the crack lengths for indentations 2 and 3.

ness experimental process, the Rockwell hardness does not require surface treatment. However, the surface should not be rough because local surface damage occurs with crack initiation which results in a hardness decrease. Factors related to a microstructure that affect the crack propagation behavior of ceramics include grain size and grain-size distribution. Other factors also include properties and distribution of bonding phase [88]. As discussed in Chapter 2, Rockwell hardness experiments performed in ceramic coatings have the potential to measure the delamination of the coating.

Three Rockwell indentations were performed at the surface APS alumina coating. The diameter of the three Rockwell indentations performed in the APS alumina specimen was measured with an optical microscope (Keyence VH-ZST) to calculate the Rockwell hardness value in the A scale (HR-A), as shown in figures 4.5(a), (b), and (c). The hardness values were calculated using equation 4.1, where h is the depth of the indentation. For the first indentation, the hardness value was around 38.95 calculated before the other indentations were made. The hardness value for indentations 2 and 3 decreased to 33.75 and 22.50, respectively. Early studies performed superficial Rockwell hardness onto APS alumina-titania coatings, ranging from 47 to 68.2 hardness value [47]. The measured Rockwell values are smaller than the hardness values from the APS alumina-titania coatings, considering the load added from the superficial Rockwell measurements. Figures 4.5(d), (e), and (f) show the depth measured with an optical microscope. The measured depth values were compared with the depth calculated using the diameter of the indentation and used to calculate the hardness values for each indentation. Figures 4.5(g) and (h) show cracks formed around indentations 2 and 3. Their fracture toughness values were computed using crack length and the Antis method [89]. Previous studies have demonstrated that the Antis method applies to ceramic materials [89]. The average crack lengths were calculated using the distance from the center of the indented region. The average crack length values are 2646.50 $\mu$m and 2720.67 $\mu$m for indentations 2 and 3, respectively. With the applied load of 588 N and the individual calculated HRA and average crack length values, indentation 2 has a fracture toughness of 2.48 MPa$\sqrt{m}$ and indentation 3 has a fracture toughness of 2.92 MPa$\sqrt{m}$. The second indentation's crack formation displays a higher number of cracks around the indented zone, indicating that the third indentation demonstrated a higher resistance to crack propagation.

$$HR = 100 - h/0.002 \tag{4.1}$$

Researchers have been able to calculate the brittleness of the ceramic material using equation 4.2 [88]. Where Hv is the measured Vickers hardness, E is the modulus of elasticity of the coating, and $K_{IC}$ is the fracture of toughness of the coating after the indentation was performed. Furthermore, previous studies have determined that Young's modulus for APS alumina coatings is 43 GPa using nanoindentation test [90].

$$B = HvE/{K_{IC}}^2 \tag{4.2}$$

### 4.3 Residual Stresses and Elastic Modulus Measured with Piezospectroscopy

In this study, the multifunctional nature of the APS alumina coating, namely the photoluminescent spectra, are used in conjunction with standard measurements. A combination of Rockwell indentation and PS were performed to determine the mechanical properties of APS aluminum oxide. The optical properties of the APS alumina coating are used to investigate the integrity of the APS alumina coating after the induced damage and to monitor the effect of the indentations across the surface of the APS alumina coating. Due to a high porosity, the APS coating has inconsistencies in the coating properties with varying location. With this in mind, nano-indentation methods would give results illustrative of the specific location, not representative of the entire coating. Macro-indentation would provide more comprehensive details for mechanical properties. Moreover, Rockwell was applicable accounting for the specimen's metallic substrate and ceramic topcoat. The PS technique was chosen for its application in capturing stress characteristics and its high resolution in data acquisition.

As discussed in Chapter 2, the lower stress values around the indented region is due to the stress being released by local damages such as delamination and vertical cracking. The average peak position of the undamaged APS coating was used as a reference value to determine the coating's peak shifts after each indentation was applied. Figure 4.6(a) show a closeup map of the first indented region with the distributed values for the peak positions. Position 1 shows the first indentation and higher peak shift values. Position 2 and 3 show lower stress values due to the stress relaxation, vertical cracks, and delamination of the coating in the indented region. Position 4 shows more stable stress values demonstrating better integrity of the coating further away from the indented region. Figure 4.6(b) show a schematic of the indented zone and the lower stress values around it affecting the coating integrity, causing delamination. Figure 4.6(c) show the stress values calculated using equation 4.3, where $\Pi$ is the stress tensor for the alumina material, $\sigma$ is the calculated stress value, and $\Delta\nu$ is the average peak position of the coating prior applying the indentations minus the peak position after the indentation was performed. The PS coefficient of 7.59 $GPa/cm^{-}1$ [91] to observe the stress changes across the samples after the indentation was applied, assuming that the coating has uniform stresses at the entire surface prior the indentations were performed.

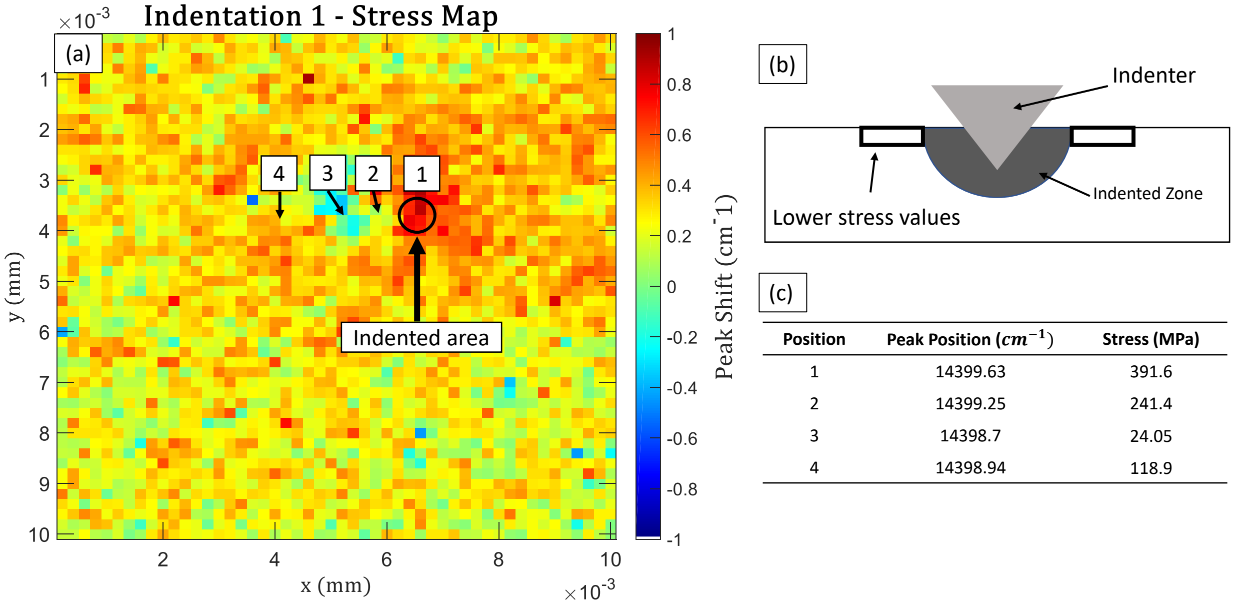

| Position | Peak Position ($cm^{-1}$) | Stress (MPa) |
|---|---|---|
| 1 | 14399.63 | 391.6 |
| 2 | 14399.25 | 241.4 |
| 3 | 14398.7 | 24.05 |
| 4 | 14398.94 | 118.9 |

Figure 4.6: (a) Contour stress map of the first indentation, (b) Schematic of the low stress values around the indented region, (c) stress values at the different locations from image (a).

Higher stress values of about 391.6 MPa, were observed at the indented location, while around the indented region, lower stress values of around 24.05 MPa were observed. Considering the brittleness of the coating, the stress changes demonstrated that the surrounding of the indented regions were affected by the load applied with the indenter.

$$\Delta\nu = \Pi_{ii} * \sigma_{jj} \tag{4.3}$$

The average peak values around the three indentations were calculated to determine the stress changes around the indented locations. Figure 4.7 show the stress changes caused by cracks can be measured using the PS technique. The diameter of every indentation was measured to locate it in the PS map, as well as the crack length. In figure 4.7 the peak values of the indented region for each indentation were averaged to determine the standard deviation and calculate the error bars. Future work can correlate this information to determine the energy absorbed by the indent. The inner and outer radius of the indents were determine using the peak positions. The inner radius represents the indentation's radius, while the outer radius represents the region affected by the indentation. The measured inner radius, Ri, for the first, second, and third indentation were 0.266 mm, 0.283 mm, and 0.322 respectively. The affected radius, Ra for the first, second, and third indentation were 2.4 mm, 3.8 mm, and 4.6mm respectively. The third indentation demonstrated to have the largest Ri and Ra considering the existing internal damages caused by the previous indentations. It is thought that due to the brittleness of the ceramic coating, internal cracks are developed after each indentation, expanding throughout the coating area.

The calculated stress values are correlated with the hardness value for each indentation. Due to the cracks observed at indentations 2 and 3, the measured hardness is smaller than indentation 1 because the affected area is much larger. Figure 4.8 shows that the stress values decreased with the size of the affected regions. The trend observed from the graph, demonstrates that the hardness and stress values decreased with the addition of the indentations. The trend observed in figure4.8 demonstrates the correlation between hardness, stress, and modulus. Considering the anisotropic behavior and heterogeneous composition of APS alumina, the coating's modulus might differ from locations. Factors such as indented location, non-melted particles, porosity and phase composition can affect the modulus measurement using indentation.

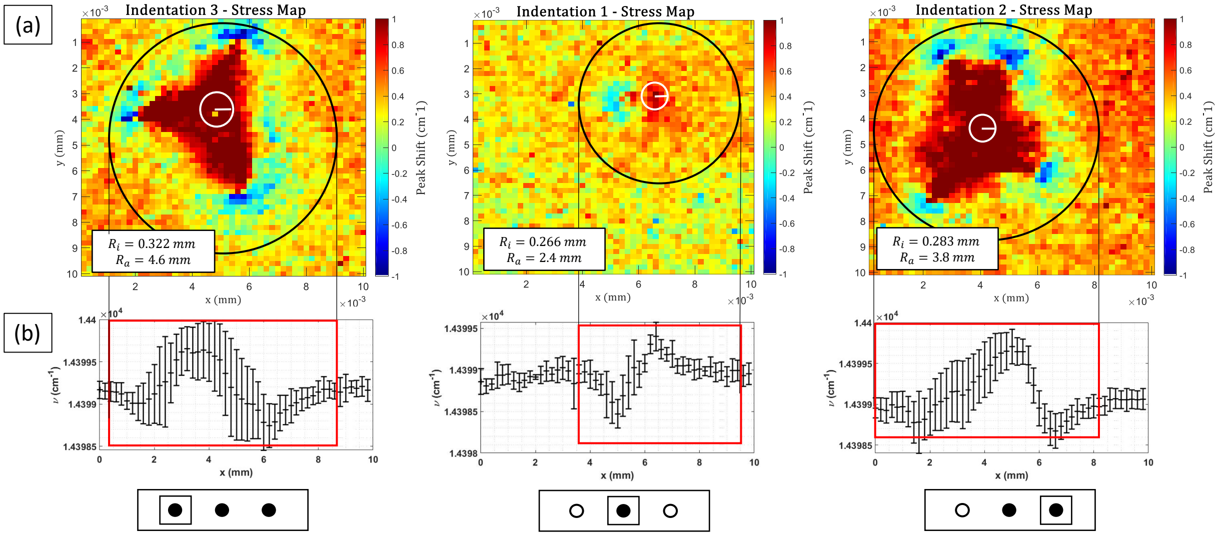

Figure 4.7: (a) Stress maps of all the indentations showing each indentation's radius (Ri) and the radius of each affected region (Ra) where peak shift values occur and (b) Graphs showing the average peak shifts between the indented and cracked locations.

After the first indentation, the Rockwell hardness value measured at the first indentation spot was found to be 38.9. The second indentation performed on the right side of the sample resulted in a Rockwell hardness value of 33.7, and the third indentation area was found to have a Rockwell hardness value of 22.5. Figure 4.8 shows the relation between the hardness value of each indentation. The second indentation area exhibited a lower hardness value likely caused by vertical cracks that could have developed due to the first indentation. The addition of each indentation was shown to affect the integrity of the coating caused by the brittleness. To determine whether other projectile regolith particles would affect the damaged coating, the hardness value of the first indentation was examined again after the third indentation was applied. The measured Rockwell hardness values were found to be affected surrounding indentations spots.

The PS measurements demonstrated that the first indentation was affected after the two indentations were performed. Each indentation was performed around 0.5 inches from each other. The ASTM E384, commonly used for hardness experiments on ceramic materials, suggest the distance between each indentation should be at least 2.5 times the size of the indentation [92]. In this experiment with higher loads than Rockwell Superficial test (45N), the indentations were performed at a spacing of 20 times more than that suggested by the standard. Figure (a) and (b) 4.9 show the peak position map of the first indentation before and after indentations 2 and 3 were performed. Comparing both images, the peak position of the first indentation increased after both indentations were performed. This is due to the cracks created during indentations 2 and 3. Figures (c) and (d) 4.9 show the intensity of the first indentation before and after the other two indentations were

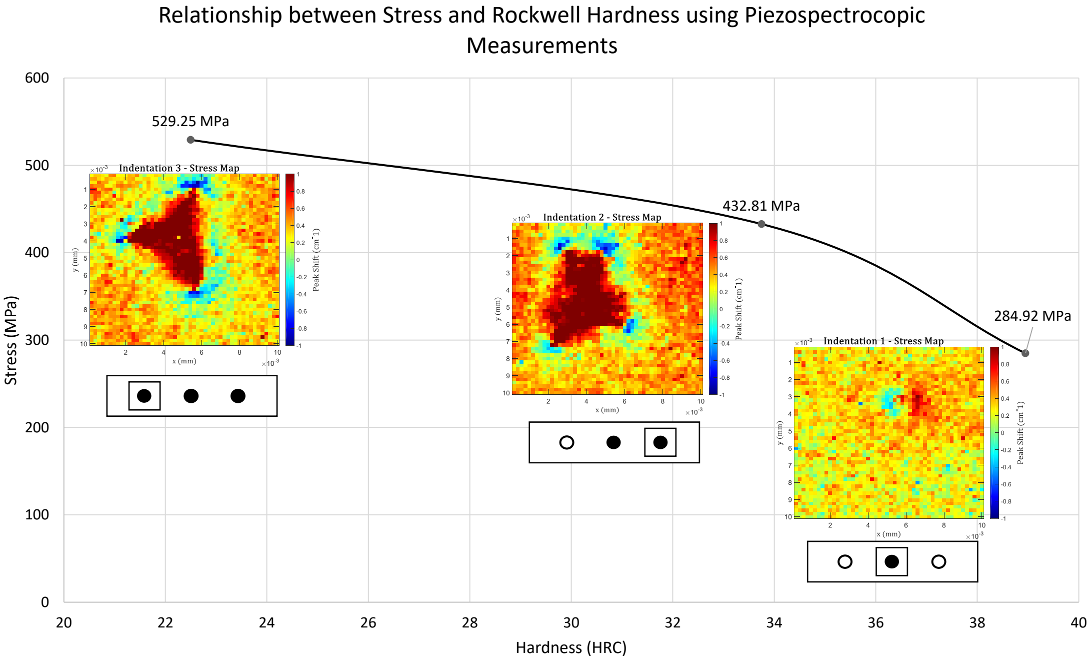

Figure 4.8: Graph relating average stress and Rockwell hardness through PS peak shifts. The stress values were calculated using the average peak shifts at the indented regions and the PS tensor, 7.59 $GPa/cm^-1$

performed. The intensity is consistent supporting the parameters and location studied for the first indentation.

The PS data collected after each indentation was performed showed that the damaged area was affected by each of the subsequent indentation. Figure 4.9 shows indentation 1 before and after the other two indentations were performed. The PS data shows the area affected around the indented region at indentation 1. Plastic deformation can be inferred around the indented region due to the increment in stress. The right figure at Figure 4.9 show higher stress values around the indented region of indentation 1. This highlights that the two indentations performed around the first indentation likely increased the plastic deformation around the first indentation.

As previously discussed, the second and third indentations affected the surroundings of the first indentation by increasing the residual stress values. In Figure 4.10(a), it is observed that after indentation 1 was applied to the coating, the coating stresses in the surrounding areas were affected. In Figure 4.10(b), it can be seen that the stress values around the first indentation increased after the second indentation was performed. The figure also shows that the indented surroundings of the second indentation were more affected compared to the first indentation. Figure 4.10(c) shows the three indentations performed and a high increase in stress values around the first indentation. The results displayed in figure 4.10, demonstrated that the distance between the regolith impacts will affect the overall integrity of the APS alumina coating. Furthermore, the PS data demonstrated the ability to collect information about the integrity of the coating and the effect of multiple impacts on the surface of the APS alumina coating.

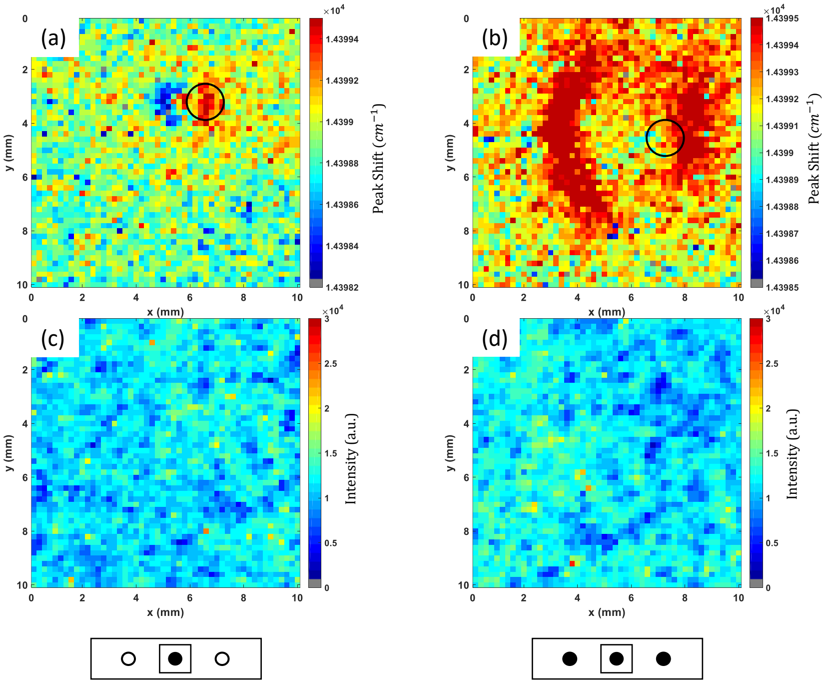

Figure 4.9: (a) Stress map of indentation 1 before the other two indentations (b) Stress map of indentation 1 after the other two indentations (c) Intensity map for the scan of indentation 1 before the other two indentations and (d) Intensity map for the scan of indentation 1 after the other two indentations.

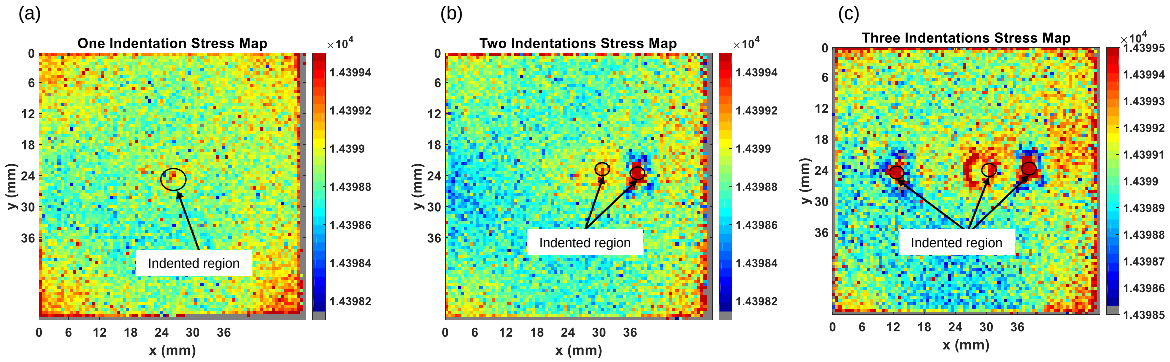

Figure 4.10: Comparison of the PS maps after each indentation was performed. (a) First indentation, (b) first and second indentations, (c) first, second, and third indentations..

# CHAPTER 5
# CONCLUSION

Providing protective coatings to ensure safety of mechanical structures for future lunar missions is of critical importance. In particular, it will be essential to protect mechanical systems from the regolith impacts and wear and abrasive damage. In this work, the low-velocity impact of regolith particles were simulated by performing quasi-static indentations. The hardness, residual stress, fracture toughness, underlying damage, and other mechanical properties were studied and analyzed. Ceramic materials have a strong background on having high strength and wear and abrasive resistance. APS alumina coating was investigated for durability using indents simulating low-impact damage points. The APS alumina coating were studied and analyzed in a series of destructive and non-destructive experiments. Experiments such as profilometry, contact angle goniometry, SEM, and XRD were performed to study the microstructural composition of the APS alumina coating. Vickers and Rockwell hardness were performed to simulate the low-velocity impacts through quasi-static indentations and determine the mechanical properties of the APS alumina coating. The Vickers hardness experiment simulated the micro-impacts, and the Rockwell simulated the macro-impacts of the lunar regolith at low-velocities. The PS technique was employed to determine the residual stresses, fracture of toughness, damage, and effects of each indentation across the surface of the coating.

Hardness values were determined using an optical microscope and measuring the diameter of the indents. The initial hardness value of the APS coating, measured at its center, was found to be 38.9 HRA and this value decreased to 22.5 HRA after two other indentations were performed on the coating. The results demonstrated that the last indentations affected the first indentation as well as the overall integrity of the coating, lowering the hardness value around 13% after the second indentation, and around 42% after the third indentation. The fracture toughness, hardness, and residual stress were determined using the Rockwell indentation method along with the PS technique. The PS data allowed the estimation of the residual stresses around the indented area and the delaminated locations. With this study, it was demonstrated that the mechanical properties can be determined using a combined method of indentation and optical techniques.

The experimental results showed that the Rockwell hardness value of the coating depends on the integrity of the surrounding coating, that can be largely affected by indentation of close-by areas. The Rockwell hardness at the initial indentation location was found to decrease as more indents were applied to the coating. The PS measurements showed the underlying damage caused by the indentation on the coating and showed that the subsequent indents were in an area of damage from the first indent causing further reduction in the integrity of the coating. The results demonstrated that the local stress and hardness values of the APS coating were found to be affected by the number of impacts and their proximity to each other.

Relating the roughness values of the coating to the indentation techniques used, it was confirmed that the roughness values can affect the hardness measurements. During the Vickers indentation experiment, measuring the indented location was difficult due to the high roughness values around the surface of the APS alumina coating. The Vickers hardness values were smaller than the values compared to literature. However, it has been demonstrated that the hardness values of thermally sprayed materials may vary due to the inconsistency of deposition method and parameter. Crack propagation might have occurred during the micro-hardness experiment due to the brittleness of the ceramic coating. Previous studies also demonstrated that the brittleness of the coating may be measured using the Vickers hardness values, the elastic modulus, and fracture toughness of the material.

For the characterizarion of the microstructural composition of the APS alumina coating, three different layer thicknesses were examined to understand the effects of the deposition process. The layer thicknesses tested were 122, 128, and 150 $\mu$m. The profilometry data demonstrated an average roughness value of 4.171, 3.714, and 4.304 $\mu$m, respectively. The layer thickness did not demonstrate a direct correlation for the roughness values. Considering the variation of roughness across the surface of the coating, the lunar regolith particle have high probabilities of adhering to the surface and cause wear and abrasive damage. The contact angle goniometer was used to measure the surface energy of the APS alumina coating, which showed that the material have high surface energy and can increase the adhesion force between the reoglith particles and the surface of the APS alumina coating. The surface energy did not demonstrate a direct relationship with the layer thickness of the coating. However, further studies will be performed to determine the relationship of greater layer thicknesses, roughness, and surface energy.

Further studies to determine the phase composition and microstrucutral integrity of the coating were performed. XRD measurements were performed to determine the phase composition at the

APS alumina coating. During the deposition process of thermally sprayed, the particles undergo a phase transition. In this study, the presence of $\alpha$- and $\gamma$-phase were expected. Higher volume fraction of $\gamma$-phase alumina was present in the APS alumina coating used in this work. However, the presence of $\alpha$-phase alumina plays an essential role due to its optical properties. Furthermore, studies have demonstrated that the presence of $\alpha$-phase alumina is more desirable due to it mechanical properties and high wear and abrasive resistance. The SEM images demonstrated micro cracks developed during the spray process, as well as splat and unmolten particles across the coating. The microstructural composition and strength of the coating may be improved considering and modifying the spraying parameters.

Further studies will be performed to study and improve the protective behavior and durability of the ceramic coating. The layer thicknesses effects on the APS alumina coating needs to be further studied and analyzed. Wear and abrasive experiments will be performed using lunar regolith simulants to determine its durability at the lunar surface. Methods to improve the manufacturing of the coating and further characterization studies will be performed to ensure these coatings provide protection and durability in the event of multiple lunar dust impact. Studies to determine multiple mechanical properties of the coating utilizing its optical properties will be performed. Future research will include studying the indentations using XRD measurements to calculate the strain changes and crack propagation during the indentation process. The adhesion forces of the lunar regolith particles on the surface of the APS alumina coatings will be analyzed as well. This effort will support future lunar missions.

# LIST OF REFERENCES

[1] D. S. McKay, G. Heiken, A. Basu, G. Blanford, S. Simon, R. Reedy, B. M. French, and J. Papike, “The lunar regolith,” *Lunar sourcebook*, vol. 567, pp. 285–356, 1991.

[2] E. Grün, M. Horanyi, and Z. Sternovsky, “The lunar dust environment,” *Planetary and Space Science*, vol. 59, no. 14, pp. 1672–1680, 2011.

[3] S. Taylor, “Chapter 12-the moon,” *Encyclopedia of the Solar System (Second Edition), Academic Press, San Diego*, pp. 227–250, 2007.

[4] W. D. Carrier III, “Particle size distribution of lunar soil,” *Journal of Geotechnical and Geoenvironmental Engineering*, vol. 129, no. 10, pp. 956–959, 2003.

[5] T. Stubbs, R. Vondrak, and W. Farrell, “Impact of electrically-charged dust on lunar exploration,” in *Space Resources Roundtable VII: LEAG Conference on Lunar Exploration*, vol. 1287, 2005, p. 85.

[6] R. L. Kobrick, D. M. Klaus, and K. W. Street Jr, “Defining an abrasion index for lunar surface systems as a function of dust interaction modes and variable concentration zones,” *Planetary and Space Science*, vol. 59, no. 14, pp. 1749–1757, 2011.

[7] J. Gaier, “The effects of lunar dust on eva systems during the apollo missions: Nasa,” *TM-2005-213610Cleveland: NASA Glenn Research Center*, 2005.

[8] Z. Ling, A. Wang, and B. L. Jolliff, “Mineralogy and geochemistry of four lunar soils by laser-raman study,” *Icarus*, vol. 211, no. 1, pp. 101–113, 2011.

[9] H. Zhang, Y. Wang, L. Chen, H. Zhang, C. Li, J. Zhuang, D. Li, Y. Wang, S. Yang, X. Li *et al.*, “In-situ lunar dust deposition amount induced by lander landing in chang’e-3 mission,” *Science China Technological Sciences*, vol. 63, pp. 520–527, 2020.

[10] I. Kuznetsov, A. Zakharov, G. Dolnikov, A. Lyash, V. Afonin, S. Popel, I. Shashkova, and N. Borisov, “Lunar dust: Properties and investigation techniques,” *Solar System Research*, vol. 51, pp. 611–622, 2017.

[11] J. Colwell, S. Batiste, M. Horányi, S. Robertson, and S. Sture, “Lunar surface: Dust dynamics and regolith mechanics,” *Reviews of Geophysics*, vol. 45, no. 2, 2007.

[12] T. Eyre, “Wear mechanisms,” *Powder Metallurgy*, vol. 24, no. 2, pp. 57–63, 1981.

[13] R. L. Kobrick, D. M. Klaus, and K. W. Street, "Developing abrasion test standards for evaluating lunar construction materials," *SAE International Journal of Aerospace*, vol. 4, no. 1, p. 160, 2009.

[14] K. M. Cannon, C. B. Dreyer, G. F. Sowers, J. Schmit, T. Nguyen, K. Sanny, and J. Schertz, "Working with lunar surface materials: Review and analysis of dust mitigation and regolith conveyance technologies," *Acta Astronautica*, 2022.

[15] M. DiGiuseppe, R. Pirich, and V. Kraut, "Lunar regolith control and resource utilization," in *2009 IEEE Long Island Systems, Applications and Technology Conference*. IEEE, 2009, pp. 1–5.

[16] C. Wohl, Y. Lin, M. Belcher, F. Palmieri, B. Atkins, and J. Connell, "Generation and evaluation of lunar dust adhesion mitigating materials," in *3rd AIAA Atmospheric Space Environments Conference*, 2011, p. 3676.

[17] R. Kruzelecky, B. Wong, B. Aissa, E. Haddad, W. Jamroz, E. Cloutis, I. Rosca, S. Hoa, D. Therriault, and A. Ellery, "Moondust lunar dust simulation and mitigation," in *40th International Conference on Environmental Systems*, 2010, p. 6023.

[18] G. Freihofer, D. Fugon-Dessources, E. Ergin, A. Van Newkirk, A. Gupta, S. Seal, A. Schulzgen, and S. Raghavan, "Piezospectroscopic measurements capturing the evolution of plasma spray-coating stresses with substrate loads," *ACS applied materials & interfaces*, vol. 6, no. 3, pp. 1366–1369, 2014.

[19] K. Ramachandran, V. Selvarajan, P. Ananthapadmanabhan, and K. Sreekumar, "Microstructure, adhesion, microhardness, abrasive wear resistance and electrical resistivity of the plasma sprayed alumina and alumina–titania coatings," *Thin Solid Films*, vol. 315, no. 1-2, pp. 144–152, 1998.

[20] A. Shonhiwa, M. Herrmann, I. Sigalas, and N. Coville, "Reaction bonded aluminum oxide composites containing cubic boron nitride," *Ceramics International*, vol. 35, no. 2, pp. 909–911, 2009.

[21] H. M. Irshad, B. A. Ahmed, M. A. Ehsan, T. I. Khan, T. Laoui, M. R. Yousaf, A. Ibrahim, and A. S. Hakeem, "Investigation of the structural and mechanical properties of micro-/nano-sized al2o3 and cbn composites prepared by spark plasma sintering," *ceramics international*, vol. 43, no. 14, pp. 10 645–10 653, 2017.

[22] P. Klimczyk, M. Cura, A. Vlaicu, I. Mercioniu, P. Wyżga, L. Jaworska, and S.-P. Hannula, "Al2o3–cbn composites sintered by sps and hpht methods," *Journal of the European Ceramic Society*, vol. 36, no. 7, pp. 1783–1789, 2016.

[23] G. Darut, F. Ben-Ettouil, A. Denoirjean, G. Montavon, H. Ageorges, and P. Fauchais, "Dry sliding behavior of sub-micrometer-sized suspension plasma sprayed ceramic oxide coatings," *Journal of thermal spray technology*, vol. 19, pp. 275–285, 2010.

[24] E. Turunen, T. Varis, S.-P. Hannula, A. Vaidya, A. Kulkarni, J. Gutleber, S. Sampath, and H. Herman, "On the role of particle state and deposition procedure on mechanical, tribological and dielectric response of high velocity oxy-fuel sprayed alumina coatings," *Materials Science and Engineering: A*, vol. 415, no. 1-2, pp. 1–11, 2006.

[25] A. Aryasomayajula, N. Randall, M. Gordon, and D. Bhat, "Tribological and mechanical properties of physical vapor deposited alpha alumina thin film coating," *Thin Solid Films*, vol. 517, no. 2, pp. 819–823, 2008.

[26] A.-M. Lazar, W. P. Yespica, S. Marcelin, N. Pébère, D. Samélor, C. Tendero, and C. Vahlas, "Corrosion protection of 304l stainless steel by chemical vapor deposited alumina coatings," *Corrosion science*, vol. 81, pp. 125–131, 2014.

[27] L. A. Johnson, "Corrosion behavior of cold sprayed aluminum oxide reinforced aluminum coatings," Ph.D. dissertation, Monterey, CA; Naval Postgraduate School, 2021.

[28] R. Fernandez and B. Jodoin, "Cold spray aluminum–alumina cermet coatings: effect of alumina content," *Journal of thermal spray technology*, vol. 27, pp. 603–623, 2018.

[29] D. Dzhurinskiy, A. Babu, S. Dautov, A. Lama, and M. Mangrulkar, "Modification of cold-sprayed cu-al-ni-al2o3 composite coatings by friction stir technique to enhance wear resistance performance," *Coatings*, vol. 12, no. 8, p. 1113, 2022.

[30] F. Kroupa, "Nonlinear behavior in compression and tension of thermally sprayed ceramic coatings," *Journal of thermal spray technology*, vol. 16, no. 1, pp. 84–95, 2007.

[31] M. Michalak, P. Sokołowski, M. Szala, M. Walczak, L. Łatka, F.-L. Toma, and S. Björklund, "Wear behavior analysis of al2o3 coatings manufactured by aps and hvof spraying processes using powder and suspension feedstocks," *Coatings*, vol. 11, no. 8, p. 879, 2021.

[32] I. Hutchings and E. Arnold, "Tribology: friction and wear of engineering materials. vol," *Metallurgy & materials science series*, 1992.

[33] L. Erickson, H. Hawthorne, and T. Troczynski, "Correlations between microstructural parameters, micromechanical properties and wear resistance of plasma sprayed ceramic coatings," *Wear*, vol. 250, no. 1-12, pp. 569–575, 2001.

[34] J. Wade, P. Claydon, and H. Wu, "Plastic deformation and cracking resistance of sic ceramics measured by indentation. in: Singh, d. and salem, j.(eds.) ceramic engineering and science proceedings. mechan-ical properties and performance of engineering ceramics and composites ix. hoboken," *NJ, USA: John Wiley & Sons, Inc*, vol. 35, no. 2, pp. 91–100, 2014.

[35] A. Manero II, A. Selimov, Q. Fouliard, K. Knipe, J. Wischek, C. Meid, A. M. Karlsson, M. Bartsch, and S. Raghavan, "Piezospectroscopic evaluation and damage identification for thermal barrier coatings subjected to simulated engine environments," *Surface and Coatings Technology*, vol. 323, pp. 30–38, 2017.

[36] R. Bantle and A. Matthews, “Investigation into the impact wear behaviour of ceramic coatings,” *Surface and Coatings technology*, vol. 74, pp. 857–868, 1995.

[37] Q. Fouliard, R. Ghosh, and S. Raghavan, “Quantifying thermal barrier coating delamination through luminescence modeling,” *Surface and Coatings Technology*, vol. 399, p. 126153, 2020.

[38] D. Clinton and R. Morrell, “Hardness testing of ceramic materials,” *Materials chemistry and physics*, vol. 17, no. 5, pp. 461–473, 1987.

[39] G. B. Ghorbal, A. Tricoteaux, A. Thuault, H. Ageorges, F. Roudet, and D. Chicot, “Mechanical properties of thermally sprayed porous alumina coating by vickers and knoop indentation,” *Ceramics International*, vol. 46, no. 12, pp. 19 843–19 851, 2020.

[40] V. Tebaldo and G. Gautier, “Influences of evaluation methods and testing load on microhardness and young’s modulus of zta and atz ceramics,” *Ceramics International*, vol. 39, no. 3, pp. 2683–2693, 2013.

[41] W. C. Oliver and G. M. Pharr, “An improved technique for determining hardness and elastic modulus using load and displacement sensing indentation experiments,” *Journal of materials research*, vol. 7, no. 6, pp. 1564–1583, 1992.

[42] B. Siebert, C. Funke, R. Va$\beta$en, and D. Stöver, “Changes in porosity and young’s modulus due to sintering of plasma sprayed thermal barrier coatings,” *Journal of Materials Processing Technology*, vol. 92, pp. 217–223, 1999.

[43] A. Vasinonta and J. L. Beuth, “Measurement of interfacial toughness in thermal barrier coating systems by indentation,” *Engineering Fracture Mechanics*, vol. 68, no. 7, pp. 843–860, 2001.

[44] E. Broitman, “Indentation hardness measurements at macro-, micro-, and nanoscale: a critical overview,” *Tribology Letters*, vol. 65, no. 1, pp. 1–18, 2017.

[45] J. Chen and S. Bull, “Approaches to investigate delamination and interfacial toughness in coated systems: an overview,” *Journal of Physics D: Applied Physics*, vol. 44, no. 3, p. 034001, 2010.

[46] J. Wang, D. Ma, and L. Sun, “The influence of crack forms on indentation hardness test results for ceramic materials,” *Journal of materials science*, vol. 50, pp. 6096–6102, 2015.

[47] T. Steeper, D. Varacalle, G. Wilson, W. Riggs, A. Rotolico, and J. Nerz, “A design of experiment study of plasma-sprayed alumina-titania coatings,” *Journal of Thermal Spray Technology*, vol. 2, pp. 251–256, 1993.

[48] Z. Yin, S. Tao, X. Zhou, and C. Ding, “Evaluating microhardness of plasma sprayed al2o3 coatings using vickers indentation technique,” *Journal of Physics D: Applied Physics*, vol. 40, no. 22, p. 7090, 2007.

[49] R. Vaßen, T. Kalfhaus, C. Vorkötter, Y. J. Sohn, S. Conze, and L.-M. Berger, "Atmospheric plasma spraying of different mgo/al2o3 feedstocks," *Journal of Thermal Spray Technology*, pp. 1–9, 2023.

[50] K. Chen, P. Song, C. Li, and J. Lu, "Influence of microstructure on hardness of plasma sprayed al2o3–tio2–mgo coatings with interface diffusion by heat treatment," *Materials Research Express*, vol. 4, no. 12, p. 126402, 2017.

[51] D. Pantelis, P. Psyllaki, and N. Alexopoulos, "Tribological behaviour of plasma-sprayed al2o3 coatings under severe wear conditions," *Wear*, vol. 237, no. 2, pp. 197–204, 2000.

[52] R. Mohammed and K. N., "Investigation of aluminium oxide coating on a216 wcb steel by plasma spraying technique," *International Journal for Research in Applied Science and Engineering Technology (IJRASET)*, vol. 8, 2020.

[53] Q. P. Fouliard, R. Ghosh, and S. Raghavan, "Thermal barrier coating delamination monitoring through thermally grown oxide spectral characterization," p. 0163, 2022.

[54] P. Jannotti, G. Subhash, J. Zheng, and V. Halls, "Measurement of microscale residual stresses in multi-phase ceramic composites using raman spectroscopy," *Acta Materialia*, vol. 129, pp. 482–491, 2017.

[55] J. Gibson, J. McKee, G. Freihofer, S. Raghavan, and J. Gou, "Enhancement in ballistic performance of composite hard armor through carbon nanotubes," *International Journal of Smart and Nano Materials*, vol. 4, no. 4, pp. 212–228, 2013.

[56] G. Bolelli, L. Lusvarghi, T. Varis, E. Turunen, M. Leoni, P. Scardi, C. L. Azanza-Ricardo, and M. Barletta, "Residual stresses in hvof-sprayed ceramic coatings," *Surface and Coatings Technology*, vol. 202, no. 19, pp. 4810–4819, 2008.

[57] P. Kaur, A. Khanna, N. Kaur, P. Nayar, and B. Chen, "Synthesis and structural characterization of alumina nanoparticles," *Phase Transitions*, vol. 93, no. 6, pp. 596–605, 2020.

[58] S.-J. Dong, B. Song, G.-S. Zhou, C.-J. Li, B. Hansz, H.-L. Liao, and C. Coddet, "Preparation of aluminum coatings by atmospheric plasma spraying and dry-ice blasting and their corrosion behavior," *Journal of thermal spray technology*, vol. 22, pp. 1222–1229, 2013.

[59] Q. Ma and D. R. Clarke, "Stress measurement in single-crystal and polycrystalline ceramics using their optical fluorescence," *Journal of the American Ceramic Society*, vol. 76, no. 6, pp. 1433–1440, 1993.

[60] I. Hanhan, E. Durnberg, G. Freihofer, P. Akin, and S. Raghavan, "Portable piezospectroscopy system: non-contact in-situ stress sensing through high resolution photo-luminescent mapping," *Journal of Instrumentation*, vol. 9, no. 11, p. P11005, 2014.

[61] X. Zhao and P. Xiao, "Residual stresses in thermal barrier coatings measured by photoluminescence piezospectroscopy and indentation technique," *Surface and Coatings Technology*, vol. 201, no. 3-4, pp. 1124–1131, 2006.

[62] B. Gill and R. Tucker, "Plasma spray coating processes," *Materials science and technology*, vol. 2, no. 3, pp. 207–213, 1986.

[63] F. Miranda, F. Caliari, A. Essiptchouk, and G. Pertraconi, "Atmospheric plasma spray processes: From micro to nanostructures," in *Atmospheric Pressure Plasma-from Diagnostics to Applications*. IntechOpen, 2018.

[64] M. S. Morsi, S. El Gwad, M. A. Shoeib, and K. F. Ahmed, "Effect of air plasma sprays parameters on coating performance in zirconia-based thermal barrier coatings," *International Journal of Electrochemical Science*, vol. 7, no. 4, pp. 2811–2831, 2012.

[65] D. Thirumalaikumarasamy, K. Shanmugam, and V. Balasubramanian, "Effect of atmospheric plasma spraying parameters on porosity level of alumina coatings," *Surface engineering*, vol. 28, no. 10, pp. 759–766, 2012.

[66] V. Viswanathan, M. J. Lance, J. A. Haynes, B. A. Pint, and S. Sampath, "Role of bond coat processing methods on the durability of plasma sprayed thermal barrier systems," *Surface and Coatings Technology*, vol. 375, pp. 782–792, 2019.

[67] V. C. Misra, Y. Chakravarthy, N. Khare, K. Singh, and S. Ghorui, "Strongly adherent al2o3 coating on ss 316l: Optimization of plasma spray parameters and investigation of unique wear resistance behaviour under air and nitrogen environment," *Ceramics International*, vol. 46, no. 7, pp. 8658–8668, 2020.

[68] P. Ananthapadmanabhan, Y. Chakravarthy, V. Chaturvedi, T. Thiyagarajan, and A. Pragatheeswaran, "Plasma-sprayed ceramic coatings for barrier applications against molten uranium corrosion," *JOM*, vol. 67, pp. 1554–1564, 2015.

[69] C. Wohl, V. Wiesner, G. King, J. Connell, and S. Miller, "Low surface energy materials for lunar dust adhesion mitigation," *The Impact of Lunar Dust on Human Exploration*, vol. 2141, p. 5014, 2020.

[70] R. Pirich, J. Weir, D. Leyble, S. Chu, and E. Taylor, "Tailoring of hydrophilic to hydrophobic coating properties for space exploration contamination control," in *41st International Conference on Environmental Systems*, 2011, p. 5066.

[71] J. Brisset, J. Colwell, A. Dove, S. Abukhalil, C. Cox, and N. Mohammed, "Regolith behavior under asteroid-level gravity conditions: low-velocity impact experiments," *Progress in Earth and Planetary Science*, vol. 5, pp. 1–21, 2018.

[72] A. Markaki and T. Clyne, "Characterisation of impact response of metallic foam/ceramic laminates," *Materials science and technology*, vol. 16, no. 7-8, pp. 785–791, 2000.

[73] A. T. Nettles and M. J. Douglas, “A comparison of quasi-static indentation testing to low velocity impact testing,” *ASTM SPECIAL TECHNICAL PUBLICATION*, vol. 1416, pp. 116–130, 2002.

[74] A. B. Hardness, “Standard test method for microindentation hardness of materials,” *ASTM Committee: West Conshohocken, PA, USA*, vol. 384, p. 399, 1999.

[75] A. I. C. E.-. on Mechanical Testing, *Standard test methods for rockwell hardness of metallic materials*. ASTM International, 2019.

[76] J. E. Colwell and M. Taylor, “Low-velocity microgravity impact experiments into simulated regolith,” *Icarus*, vol. 138, no. 2, pp. 241–248, 1999.

[77] G. Freihofer, L. Poliah, K. Walker, A. Medina, and S. Raghavan, “Optical stress probe: in-situ stress mapping with raman and photo-stimulated luminescence spectroscopy,” *Journal of Instrumentation*, vol. 5, no. 12, p. P12003, 2010.

[78] Q. P. Fouliard, R. Ghosh, and S. Raghavan, “Delamination of electron-beam physical-vapor deposition thermal barrier coatings using luminescent layers,” in *AIAA Scitech 2021 Forum*, 2021, p. 0432.

[79] P. Latorre-Suarez, K. Gucwa, O. Swaby, L. Bansberg, Q. Fouliard, and S. Raghavan, “Indentations and optics: A method to determine hardness, stress, and young’s modulus,” *Submitted for publication, in review*, 2022.

[80] S. Raghavan, P. Imbrie, and W. A. Crossley, “Spectral analysis of r-lines and vibronic sidebands in the emission spectrum of ruby using genetic algorithms,” *Applied spectroscopy*, vol. 62, no. 7, pp. 759–765, 2008.

[81] I. Maslenikov, A. Useinov, A. Birykov, and V. Reshetov, “Reducing the influence of the surface roughness on the hardness measurement using instrumented indentation test,” in *IOP Conference Series: Materials Science and Engineering*, vol. 256, no. 1. IOP Publishing, 2017, p. 012003.

[82] X.-Y. Jiang, J. Hu, S.-L. Jiang, X. Wang, L.-B. Zhang, Q. Li, H.-P. Lu, L.-J. Yin, J.-L. Xie, and L.-J. Deng, “Effect of high-enthalpy atmospheric plasma spraying parameters on the mechanical and wear resistant properties of alumina ceramic coatings,” *Surface and Coatings Technology*, vol. 418, p. 127193, 2021.

[83] Y. Gao, M. Jie, and Y. Liu, “Mechanical properties of al2o3 ceramic coatings prepared by plasma spraying on magnesium alloy,” *Surface and Coatings Technology*, vol. 315, pp. 214–219, 2017.

[84] K. Sabiruddin, J. Joardar, and P. Bandyopadhyay, “Analysis of phase transformation in plasma sprayed alumina coatings using rietveld refinement,” *Surface and Coatings Technology*, vol. 204, no. 20, pp. 3248–3253, 2010.

[85] P. Chraska, J. Dubsky, K. Neufuss, and J. Pisacka, “Alumina-base plasma-sprayed materials part i: Phase stability of alumina and alumina-chromia,” *Journal of thermal spray technology*, vol. 6, pp. 320–326, 1997.

[86] P. Zamani and Z. Valefi, “Microstructure, phase composition and mechanical properties of plasma sprayed al2o3, cr2o3 and cr2o3-al2o3 composite coatings,” *Surface and Coatings Technology*, vol. 316, pp. 138–145, 2017.

[87] V. Koshuro, A. Fomin, and I. Rodionov, “Composition, structure and mechanical properties of metal oxide coatings produced on titanium using plasma spraying and modified by micro-arc oxidation,” *Ceramics International*, vol. 44, no. 11, pp. 12 593–12 599, 2018.

[88] E. Medvedovski and P. Sarkar, “Indentation testing of structural ceramics,” *Am. Ceram. Soc. Bull.*, vol. 82, no. 12, pp. 9201–9213, 2003.

[89] L. Ćurković, V. Rede, K. Grilec, and A. Mulabdić, “Hardness and fracture toughness of alumina ceramics,” in *12th Conference on Materials, Processes Friction and Wear*. Citeseer, 2007, pp. 21–23.

[90] O. Kovářík, J. Siegl, J. Nohava, and P. Chraska, “Young’s modulus and fatigue behavior of plasma-sprayed alumina coatings,” *Journal of thermal spray technology*, vol. 14, no. 2, pp. 231–238, 2005.

[91] J. He and D. R. Clarke, “Determination of the piezospectroscopic coefficients for chromium-doped sapphire,” *Journal of the American Ceramic Society*, vol. 78, no. 5, pp. 1347–1353, 1995.

[92] G. Quinn, “Indentation hardness testing of ceramics.” *Materials Park, OH: ASM International, 2000.*, pp. 244–251, 2000.